Environmental Fluid Mechanics (2023) 23:965–1010
https://doi.org/10.1007/s10652-023-09943-z

ORIGINAL ARTICLE

Experimental investigation and integral simulation of a thermal annular plume

Maria K. Stefanidou[1] · Aristeidis A. Bloutsos[2] · Panayotis C. Yannopoulos[1]

Received: 4 December 2021 / Accepted: 5 August 2023 / Published online: 8 September 2023

Abstract

Thermal plumes issued with mean exit velocities of 0.527 and 0.702 m/s from internally closed annular nozzles are investigated experimentally, theoretically, and numerically. The experimental setup and the measurement and analysis methodologies for flow and mixing are described in detail. The experimental setup consists of an air heating box with an annular slot of 0.12-m mean diameter and 0.01-m width, accompanied by equipment for setup operation and measurement of mean velocities and temperatures. The trajectory of maximum velocities and the isovelocity contours indicate reattachment due to plume self-merging at $z_{P0} = 0.161$ m and around 0.20 m in correspondence to exit velocities. It was found that z_{P0} depends mainly upon initial Froude number and annulus equivalent diameter. Experiments detected a vortex ring right after the exit followed by a stagnation point at $z_{P1} \cong 0.055$ m on the plume centreline. The annular plume core obtains almost uniform temperature and on average 15 times higher dilutions than bulk dilutions of the equivalnt round plume. To predict the self-merging trajectory, a novel integral model was developed named self-merging approach (SMA). SMA is based on the solution of the ordinary differential equations of momentum and buoyancy applied to an infinitesimal sector of the annular plume, which is equivalent to two identical slot plumes. These plumes are reattached due to outer entrainment, inner entrainment starvation, and a series of sinks along the annular plume centreline with strengths calculated by an original relationship. SMA predictions agree very well with the observations. The present findings contribute to a better understanding of the phenomenon and offer new ideas for designing buoyancy-operating disposal systems with low momentum, using annular- or rosette-type diffusers mainly in shallow water bodies.

✉ Panayotis C. Yannopoulos
yannopp@upatras.gr

Maria K. Stefanidou
mstefanidou@upatras.gr

Aristeidis A. Bloutsos
abloutsos@uniwa.gr

[1] Environmental Engineering Laboratory, Department of Civil Engineering, University of Patras, 265 04 Patras, Greece

[2] Hydraulics and Geotechnical Engineering Division, Department of Civil Engineering, University of West Attica, 122 43 Athens, Greece

Key points

- Novel prediction of annular plume reattachment assuming a pair of plane plumes with inner entrainment starvation
- The reattachment distance increases proportionally with initial Froude number and equivalent diameter of the annulus
- Excellent integral model predictions for centreline velocities and concentrations beyond the core of annular plume

Keywords Ring plume reattachment · Vortex ring · Stagnation point · Integral model · Velocity and temperature measurement · Conformal mapping

1 Introduction

Non-isothermal fluids may initiate flows due to the temperature differences, which induce buoyant forces, as the density depends on temperature. Thus, heat sources in fluid environments will form thermal plumes due to natural convection [1]. Oftentimes, a thermal plume is a combined result of strong buoyancy under weak inertia, due to considerable different temperatures from the surrounding fluid and initial low momentum [2]. Therefore, plumes as flows where buoyancy dominates present similar flow characteristics. Thermal plumes convect thermal energy and, in many cases, carry, diffuse, and disperse various pollutants either emitted from the heat sources themselves or produced by chemical reactions in fluid environments. Thermal plumes are found both in nature and in human-originated releases. Well-known cases include: (a) Releases of gases in the atmosphere during volcanic eruptions or from earth faults [3–5]; (b) emissions of gaseous thermal pollutants in the troposphere from chimneys or cooling towers [6, 7]; (c) pollutant discharges from diffusers during the disposal of wastewater, brine discharges from desalination plants or thermal effluent discharges in the ocean [8–10].

One of the main reasons for studying the behaviour of thermal plumes is to mitigate their environmental impact. Engineering examples in wastewater disposal have been given by Fischer et al. [8], Roberts et al. [11], and elsewhere. In the troposphere and in aquatic environments, the temperature increase with height causes stratification, which may contribute to the entrapment of pollutants conveyed by plumes, resulting in adverse effects on humans and ecosystems. Some researchers consider thermal plumes to test fire models [12, 13] by simulating the spreading of fire smoke and toxic gases, aimed at helping designers and security engineers develop fire safety precautions and systems. In addition, the study of thermal plumes may help in the improvement of the ventilation systems in buildings [14–17]. Generally, in practical applications, the mean flow and mixing characteristics are among the most useful for better understanding and/or decision making.

The annular plume is a limiting case of the annular buoyant jet. Figure 1 depicts a general configuration of flow and mixing. Although the flow and mixing coming from annular jets have been extensively studied in the last 50 years by several researchers [18–26], specific studies focusing on annular plumes are very limited. The special case of ventilated annular jets, which had the inner space of the annular nozzle open in the atmosphere, has been experimentally investigated by Warda et al. [22] and Padhani et al. [26]. Wang et al. [27] have numerically simulated thermal annular plumes of four different ratios (outer

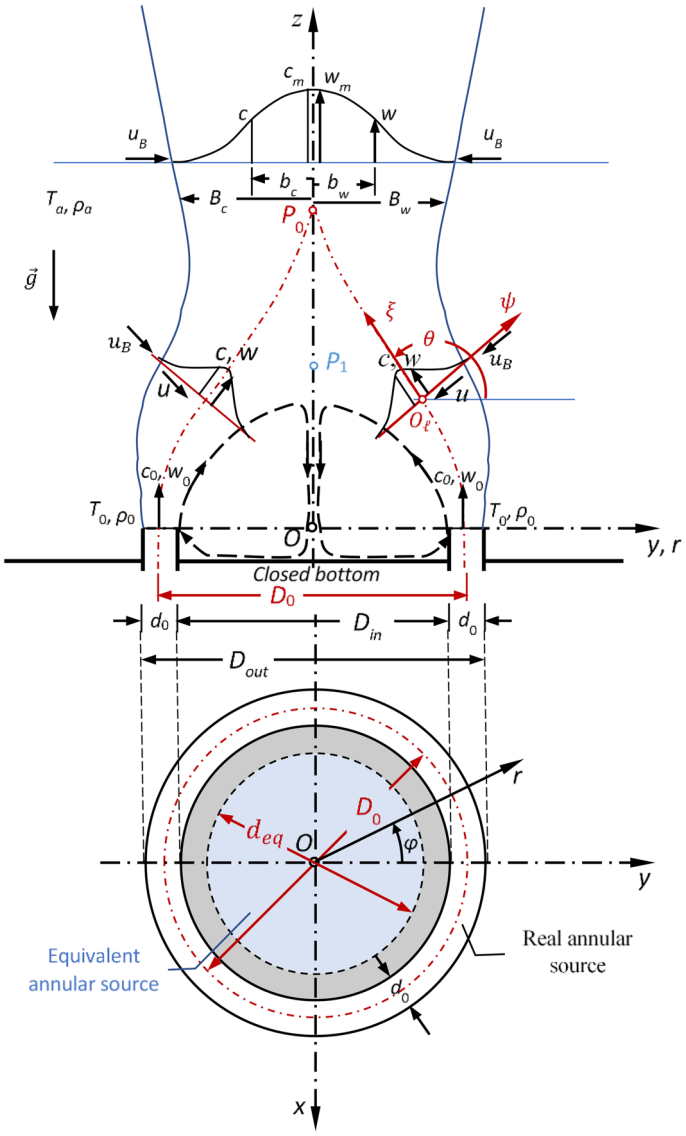

Fig. 1 Configuration of thermal plume flow and mixing coming out from a horizontal annular source (or ring exit) of mean diameter D_0 and width d_0, internally closed, in a calm ambient environment; the vortex ring, the equivalent annular source of diameter d_{eq} and the main Cartesian and cylindrical coordinate systems are depicted

diameter over inner diameter of the annulus: 5/1, 5/2, 5/3, 5/4) using FLUENT CFD combined with the realizable k-ε turbulence model and standard wall function. Their study has provided useful implications regarding the mean flow characteristics.

It is important to underline that a plume, being the limiting behaviour of a buoyant jet with strong buoyancy and weak momentum, becomes vertical right after the exit, irrespective of the nozzle inclination. Therefore, an annular plume may be considered as the

limiting case of a series of plumes forming a rosette-type diffuser, which consists of the maximum possible number of nozzles. Rosette-type diffusers with four or more ports have been investigated by several researchers [28–33]. The configuration details of rosette-type diffusers constitute an interesting engineering topic, because they may affect initial dilutions in shallow water bodies [31, 32].

Alternatively, the annular plume could be considered as the limiting case of a coaxial plume with a very small flow rate from the central nozzle compared to the flow rate from the outer annular nozzle, which discharges fluid with dominant buoyancy over momentum. Favre-Marinet and Schettini [34] have experimentally investigated the density field of coaxial jets with large density differences; they have concluded that buoyancy effects are negligible on mixing in the near field region of coaxial jets. Regarding annular jets, they have declared that no further experiments have been carried out to explore the near-field and the striking behaviour of the gravity-aided annular jet remains so far unexplained. A similar finding is indirectly indicated from the results provided by Li et al. [35] and Li and Flynn [36], who have examined coaxial plumes.

For a thermal annular buoyant jet, the dimensionless relative temperature at (x, y, z) of the fluid is defined as $c = \Delta T/\Delta T_0 \cong \Delta\rho/\Delta\rho_0$ when $\rho_a/\rho_0 \cong 1$. Thus, c is also about equal to the relative concentration based on fluid densities owned to fluid temperatures and it will be hereinafter also called relative concentration or briefly concentration; $\Delta T = T - T_a$; $\Delta\rho = \rho_a - \rho$; $\Delta T_0 = T_0 - T_a$; $\Delta\rho_0 = \rho_a - \rho_0$; T, ρ mean temperature and mean density at (x, y, z); T_0, ρ_0 and T_a, ρ_a are the fluid temperatures (K or °C) and densities (kg m^{-3}) at the plume exit and ambient environment, correspondingly. Application of the dimensional analysis (DA) helps in a concise presentation of the results in diagrams. Many researchers have used DA for deriving empirical laws of relevant flow and mixing problems, to give but some [8, 37, 38].

Experiments have shown that the flow of a thermal annular plume is determined uniquely by the quantities B_0, m_0, ν, a_T, D_{out}, D_{in}, P_{atm}/ρ_a and z, which form a set of eight independent variables, where $B_0 = g_0' A_0 w_0 c_0$ is the initial kinematic buoyancy flux (m^4 s^{-3}), $g_0' = g\beta\Delta T_0$ or, alternatively, $g_0' = g\Delta\rho_0/\rho_0$ is the effective gravitational acceleration (m s^{-2}), $\beta = T_a^{-1}$ is the volumetric temperature expansion coefficient (K^{-1}); $A_0 = \pi d_{eq}^2/4$ is the cross-sectional area (m^2) of the source, w_0 and c_0 are the mean exit velocity (m/s) and relative temperature or concentration of the fluid at the exit; $c_0 = 1$; $m_0 = A_0 w_0^2$ is the initial kinematic momentum flux (m^4 s^{-2}); ν is the fluid kinematic viscosity (m^2/s); a_T is the fluid thermal diffusivity (m^2/s) defined as the ratio of thermal conductivity k (W m^{-1} K^{-1}) over the product of the fluid density ρ (kg m^{-3}) times the specific heat c_p (J kg^{-1} K^{-1}), i.e. $a_T = k(\rho c_p)^{-1}$; D_{out}, D_{in} are the outer and inner diameters of the annular source or ring exit; P_{atm}/ρ_a is the kinematic atmospheric pressure; and z is the vertical distance from the source. Following Fischer et al. [8], a characteristic length scale d_{eq} (m) is defined as $d_{eq} = 2\sqrt{A_0/\pi} = 2\sqrt{D_0 d_0}$, where $D_0 = (D_{out} + D_{in})/2$ is the mean diameter and $d_0 = (D_{out} - D_{in})/2$ is the width of the annular slot. It is also necessary to define the inner area of the annulus $A_{in} = \pi D_{in}^2/4$. The above set of variables contains only dimensions of length and time, and formal DA would indicate that there are only six truly independent dimensionless groups, which may be formed from the set of variables. The six groups are: The local Rayleigh number $Ra = g_0' z^3 \nu^{-1} a_T^{-1}$, the initial Froude number $F_0 = w_0/\sqrt{g_0' d_{eq}}$, the initial Reynolds number $Re = w_0 d_{eq} \nu^{-1}$, the dimensionless initial pressure $F_{m0} = m_0 (A_{in} P_{atm}/\rho_a)^{-1}$, the ratio D_{out}/D_{in}, and the dimensionless axial distance z/d_0 or the normalised dynamic axial distance $Z = z/(d_{eq} F_0)$. Therefore, for the present study that

examines a thermal annular plume, the variations of mean flow and mixing quantities can be fully described with respect to the dimensionless independent variables z/d_0 or Z, D_{out}/D_{in}, F_0, Re, F_{m0} and Ra. The kinematic buoyancy flux is equal to $B_0 = (\pi/4)F_0^{-2}d_{eq}w_0^3$.

The behaviour of a thermal plume is laminar for values of Rayleigh number $Ra < 9 \times 10^6$ and it becomes turbulent when $Ra > 9 \times 10^6$ [39]. Regarding the annular plume of the present study, it will be seen below that the plume is turbulent in the whole region of the flow field due to the special formation of the device and because Re is higher than or approximately 1000. Therefore, the mean flow and mixing quantities will only depend on z/d_0 or Z, D_{out}/D_{in}, F_{m0} and F_0. However, the dimensionless pressure F_{m0} at the inner boundary of the annular plume only affects the flow properties close to this boundary. In regions beyond the core, for presentation independence of the experimental data and model predictions, length variables are normalised by dividing them by $l_n = d_{eq}F_0$. Velocities and concentrations (including relative temperatures) are normalised by dividing them by $w_n = w_0F_0^{-1}$ and $c_n = c_0F_0^{-1}$, correspondingly. In the core region, nondimensionalisation of the length variables is made by dividing them either by D_{out} or d_0, of velocities by w_0 and concentrations or relative temperatures by c_0. For the present experimental case, the Pèclet number $Pe = w_0d_{eq}a_T^{-1}$ is of order 1000 ($Pe >> 10$); thus, the transport due to thermal diffusion is expected to be practically insignificant compared to the transport due to convection [40].

The present study examines the flow field of an annular thermal plume experimentally, theoretically, and numerically. The experimental investigation deals with the trajectory of the self-merging of the annular plume and important characteristics in the near field, including the mean axial velocities and mean concentrations along the trajectory and the centreline in the core region and beyond. The core region of the thermal annular plume is defined as the zone right after the exit and up to the complete merging of the plume. Beyond the core region, the annular plume behaves like an equivalent round plume. The theoretical investigation concerns the development of a novel integral model, named self-merging approach (SMA). Using SMA, the self-merging trajectory, as well as the mean axial velocities and mean concentrations along the annular plume centreline, are predicted and compared to the experimental observations. From SMA predictions and their comparisons, useful conclusions are derived, which may help engineers and other scientists to better understand the phenomenon and optimise the design and operation of related effluent systems. In addition, a sensitivity analysis on the integral model's predictions is presented and practical implications are discussed.

2 The laboratory experiments

The experiments were carried out in a room space at the Environmental Engineering Laboratory (EEL), Department of Civil Engineering, University of Patras, Greece. The experimental space was demarcated with two vertical semi-cylindrical Plexiglas walls, forming a chamber as shown in Fig. 2.

A metallic frame supported the walls leaving a gap beneath them, above the floor, and another gap over the walls up to the ceiling, allowing air interchange between the room and the chamber. The experimental setup was placed in the middle of a room of 50-m^2 area and 2.89-m height. The floor altitude is 73 m above sea level. The air conditioning system was turned off and the door and windows were kept closed during the measurements, to prevent flow disturbances. During the measurement periods, the room air temperature

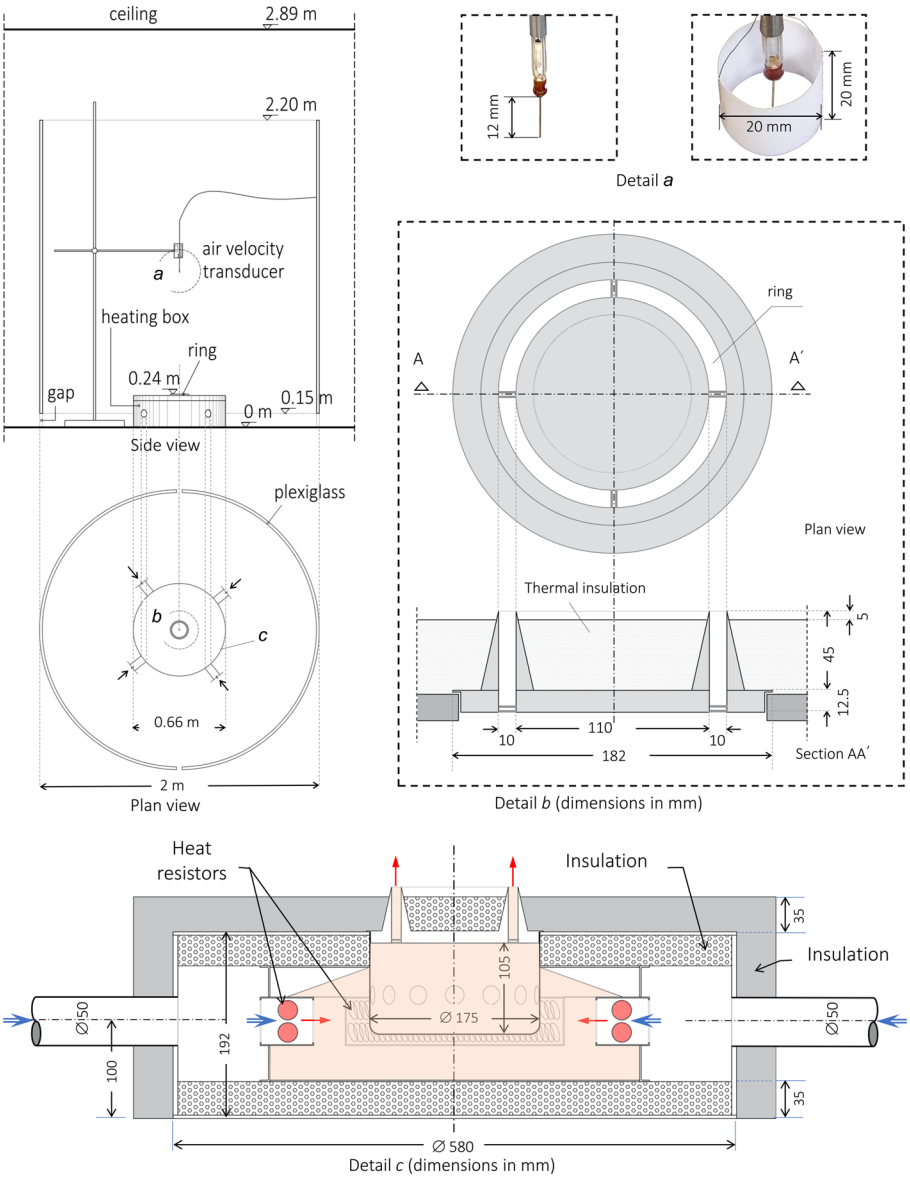

Fig. 2 Side view, plan view and required details of the experimental chamber and the thermally insulated heating box with the annular nozzle. The open arrows show the cold air route and the solid arrows the hot air route; the hot air occupies the light shadowed region of the air heating box (detail **c**) and comes out from the ring exit of the annular nozzle forming a turbulent annular plume

varied seasonally from 16 to 33 °C and the relative humidity from 40 to 65%. The mean diameter and the width of the ring exit were $D_0 = 0.12$ m and $d_0 = 0.01$ m, correspondingly, and the area of the ring exit was $A_0 = 37.7$ cm^2; the mean air temperature at the exit was 68.5 °C, the flow rate was either $\mu_0 = 1.986 \times 10^{-3}$ or 2.646×10^{-3} m^3/s, the

initial effective acceleration ranged from $g'_0 = 1.14$ to 1.78 m s^{-2}, the kinematic buoyancy flux from $B_0 = 2.264 \times 10^{-3}$ to 4.176×10^{-3} m^4 s^{-3} and the initial Froude number from $F_0 = 1.50$ to 2.12.

The experimental setup and its main parts are schematically presented in Fig. 3. The setup includes an air compressor electronically controlled by a Venturi meter and set to the desired flow rate. The air heating box includes four air resistors of 500-W power each, installed within the box right after each of the four air entrances linked with the air compressor through flexible PVC ducts of 50-mm diameter. The box was sufficiently insulated to prevent heat losses and avoid secondary air flows. The route of the air in the box is labyrinthine (meandering). After the air enters the box, the air flow passes through the resistors and becomes hot; then, it enters through the 14 holes of 19-mm diameter each opened around the pot underneath the annulus and exits out from the annular slot. Due to this route of air flow and since the diameter of the pot is significantly longer than that of the ring exit (detail c in Fig. 2), air vortices are generated, and the air flow becomes turbulent, as this formation behaves like the "Cooper" nozzle [41]. The power of the resistors is controlled by an electronic power controller, which senses the mean air temperature within the box and regulates the air temperature at the desired level. The air velocity transducer, model 8465 TSI, was used for velocity measurements. The temperature range of the transducer is [0–93] °C. For the velocity measurements of the present work [0.125–1.5] m/s, the error was less than 10% of the reading. However, it is important to point out that this meter cannot distinguish the velocity direction and it can correctly measure the flow velocity when it is directed parallel to the sensor needle. It is observed that in regions away from the plume centreline, where there are vortices and/or entrainment, the measured velocity magnitudes were found higher than the real ones. In these regions, this effect was partly reduced by installing the transducer within a cardboard hollow cylinder of 2-cm diameter and 2-cm height, as proposed by Stefanidou et al. [42] and shown in the detail a of Fig. 2. A pen laser was placed permanently next to the sensor to mark on the horizontal surface of the

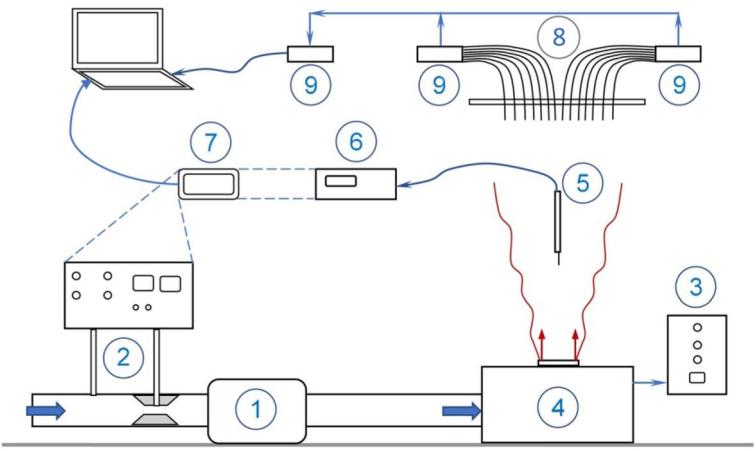

Fig. 3 Main parts of the experimental setup: 1. Air compressor; 2. Venturi measuring system and air discharge display; 3. air heating regulator; 4. air heating box with an annular nozzle; 5. velocity transducer; 6. air velocity display; 7. video camera for recording measurement values and transfer to computer for processing; 8. Two series of 14 thermistors; 9. Signal receivers, transfer, and communication with the computer for processing

air heating box the distance of the sensor location from the vertical z axis and a small spirit level was used to achieve the verticality of the sensor. The sensor was mounted on a support system that could be moved horizontally and vertically. A video camera was used to record measurement values displayed on the transducer screen; then, the measurements were downloaded on a computer for further processing.

Two series of totally 14 J-type thermocouples for temperature measurements were fixed on a horizontal metal rod at the vertical symmetry plane of the annular plume. The system was able to move in the vertical direction sliding on the two vertical metal brackets and could be fixed at the desired level required for the measurements. The signals of measurements were received from electronic devices and transferred to the computer for processing. The air temperatures at the exit and the background were measured using the HH147 OMEGA Data Logger Thermometer with four thermocouples of K type with a resolution of 0.1 °C in the range $(-100, 200)$ °C and accuracy $\pm$ (0.1% reading +0.7 °C). At two background locations of the chamber around the middle height level, as well as at several locations and levels of the room space, the temperature was measured at several characteristic instances during the measurements, using common thermometers. A schematic presentation of the axial velocity and temperature measurement system is depicted in Fig. 3, while additional details on measurements are provided in "Appendix 2".

3 Theoretical considerations

3.1 Basic assumptions and governing equations

A thermal plume coming from a horizontal annular source with initial velocity w_0, temperature T_0 and density ρ_0 is considered. The fluid is discharged in a motionless and uniform ambient environment of temperature T_a and density ρ_a in steady state conditions. The internal region of the plume, after the ring exit, is sealed off from the outer environment. Due to symmetry conditions, the entrainment from the inner core region of the annular plume is self-nulled. It will be shown that the outer entrainment in conjunction with the inner entrainment starvation and the flow potential induce the Coandă effect, which contributes to plume contraction and reattachment at P_0 (Figs. 1, 4). Furthermore, a vortex ring is induced by the shear stresses imposed by the velocity field of the annular plume in the inner core region. Three coordinate systems are defined: The basic Cartesian (O, x, y, z); the cylindrical (O, r, φ, z); and the local 2D orthogonal curvilinear coordinate system (O_l, ψ, ξ), where z is vertical and ξ follows the curvilinear axis of the annular plume, which is defined as the locus of maximum velocities; the ξ axis begins from the slot centre of the ring exit and ends up at the merging point P_0 at the plume centreline; O_l is the origin of the local ψ-axis, which is perpendicular to the ξ-axis; the plane (ψ, ξ) is vertical.

The equations of volume, momentum, and tracer conservation are derived based on the usual assumptions and approximations, namely (a) the Boussinesq approximation made for small initial density differences, (b) the Prandtl's boundary-layer-type approximation, (c) the neglect of the molecular viscosity terms, and (d) the absence of swirl. In addition, second-order terms for the turbulence contribution to momentum and buoyancy fluxes are included [43–45]. The present theoretical work is going to examine the phenomenon in steady-state conditions under a novel approach, which dares to simulate and predict among others the self-merging of the annular plume. Considering that the phenomenon is axisymmetric with respect

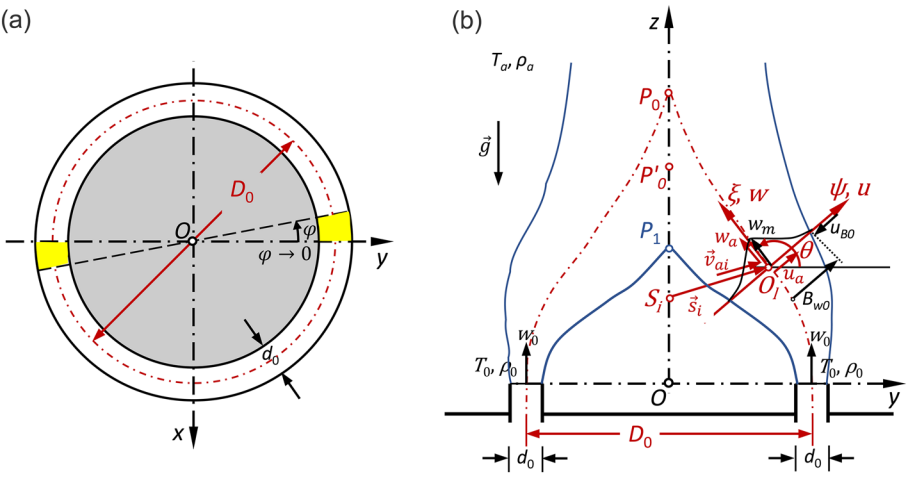

Fig. 4 Sketches explaining the equivalence between **a** two symmetrical infinitesimal sectors of the ring exit and **b** two plane plumes originating from identical slots of width d_0 and equal initial velocity, temperature and density to the annular plume; entrainment velocity u_{B0} at outer boundary B_{w0}, flow potential $\vec{v}_{ai}$ due to infinite number of sinks S_i along annular plume centreline Oz, reattachment point P_0, stagnation point P_1, and point P'_0 where centreline velocity is maximised are also shown

to the vertical axis z, the steady-state partial differential equations (PDE) are synoptically written below to fit to the coordinate systems mentioned above:

continuity

$$\frac{\partial(r^i hu)}{\partial r_i} + \frac{\partial(r^i w)}{\partial z_i} = 0; \tag{1}$$

ψ-momentum

$$\begin{aligned}\frac{\partial[(r\sin\varphi)^i hu^2]}{\partial r_i} + \frac{\partial[(r\sin\varphi)^i(uw - \tau_{rz_i}/\rho_0)]}{\partial z_i} - r^i\left(w^2 + w'^2 + \frac{p_d}{\rho_0}\right)\frac{\mathrm{d}\theta}{\mathrm{d}z_i} \\ = -g'_0 r^i hc\cos\theta - \frac{\partial[(r\sin\varphi)^i hp_d]}{\rho_0 \partial r_i};\end{aligned} \tag{2}$$

z_i-momentum

$$\begin{aligned}\frac{\partial(r^i huw)}{\partial r_i} + \frac{\partial[r^i(w^2 + w'^2 + p_d/\rho_0)]}{\partial z_i} + (r\sin\varphi)^i\left(uw - \frac{\tau_{rz_i}}{\rho_0}\right)\frac{\mathrm{d}\theta}{\mathrm{d}z_i} \\ = g'_0 r^i hc\sin\theta + \frac{\partial(r^i h\tau_{rz_i})}{\rho_0 \partial r_i};\end{aligned} \tag{3}$$

tracer

$$\frac{\partial(r^i huc)}{\partial r_i} + \frac{\partial[r^i(wc + w'c')]}{\partial z_i} = -\frac{\partial(r^i hu'c')}{\partial r_i}. \tag{4}$$

In PDE (1)–(4), $i = 0$ for the 2D system; and $i = 1$ for the normal cylindrical system; u and w are the mean velocity components in the directions either $r_0 \equiv \psi$ and $z_0 \equiv \xi$ of the 2D orthogonal curvilinear system or $r_1 \equiv r$ and $z_1 \equiv z$ of the normal cylindrical system; $h = 1 + \psi \mathrm{d}\theta/\mathrm{d}\xi$ and $h = 0$ the scale factor of the 2D and cylindrical coordinate systems, correspondingly; θ is the local inclination of ξ-axis; $\tau_{rz_i} = -\rho u'w'$ is the mean turbulent shear stress acting on the rz_i plane; w'^2, $u'w'$, $w'c'$, $u'c'$ are the mean local fluxes due to turbulence fluctuations of w, u, c; p_d is the mean dynamic pressure.

It is useful to briefly describe the superposition method (SM), which is used for comparisons with SMA in Sect. 4. SM is an integral method, which can be applied in groups of interacting either pure jets or plumes [44, 46]. SM application presents several advantages for both pure jets and plumes. Regarding pure jets, the fluxes of momentum and tracer are conserved, and the PDE of momentum becomes linear with respect to the squared mean axial velocities. Regarding plumes, the fluxes of the centreline gradient of the mean-flow kinetic energy and the tracer or buoyancy are conserved and the PDE of mean flow kinetic energy becomes linear with respect to the third power of the mean axial velocities. More recently [47, 48], SM was extended to apply to finite area sources (like plane, round, or annular plumes), assuming that these sources are composed by an infinite number of point or line sources. This extension is based on the above mentioned linearity of the PDE of mean flow kinetic energy along with the conservation of the tracer or buoyancy flux.

3.2 Modelling the self-merging of the annular plume

The annular-plume merger phenomenon can be approximated by considering the merging of two symmetrical infinitesimal sectors (sector plumes or side-plane plumes) of the annular plume. This approximation can be easily explained if we pay attention to Fig. 4. A plan view of the annular source is shown in Fig. 4a. Another simple and intuitive explanation could be just unrolling a belt. If we draw the vertical planes containing two diameters, we can separate two symmetrical infinitesimal sectors of the ring exit and the flow field of two plane plumes corresponding to the same angle $\varphi \to 0$. A strictly mathematical justification of the self-merging of the annular plume to resemble that of two-plane plumes is based on the method of conformal mapping and is described in "Appendix 3". This method enables to determine the region of validity of SMA, which is for $d_0/D_0 \leq 0.31$ or, equivalently, the range $1 < D_{out}/D_{in} < 2$. The following conditions are valid: (a) the annular source has a relatively low value of d_0/D_0, practically $d_0/D_0 \leq O(0.1)$; *b*) all flow properties at both cross-sectional areas of each sector are correspondingly equal and also the vertical planes defining the sectors constitute symmetry planes; *c*) the fluxes corresponding to these sector plumes are e(ual to those of the annular plume after dividing them by the local equivalent plume perimeter, thus referring to a 2D-flow field; (d) the sector plumes entrain fluid only from their outer boundaries, since the inner space between them is entirely closed and the inner entrainment is interchanging among their inner boundaries; the inner entrainment induced by the vortex ring near the exit is detrained by the same vortex ring and circulates in the vortex region; thus, the inner entrainment may be ignored; (e) a pressure deficit exists between the external ambient fluid and the annular core and this deficit draws the annular plume towards the centreline. The annular plume contracts to a circular plume quickly and does not maintain its ring nature for an extended time. Thus, the sector plume trajectory is controlled by the combined effect of the outer entrainment and the reciprocal attraction between the two sector plumes.

Therefore, the two symmetrical infinitesimal sector plumes shown in Fig. 4a are considered equivalent to two plane plumes having the same initial characteristics with those of the annular plume shown in Fig. 4b. These plane plumes entrain fluid from the surroundings and their volume flux is increasing with z because of plume expansion and satisfaction of the continuity equation. They are also subjected to a flow potential [49, 50] induced by a series of sinks $S_i (i = 1, N)$ of volume strength $\delta\mu_1$ located on the annular plume centreline Oz (Fig. 4b). Batchelor [49] has shown that velocities imposed at a point O_l of the plane plume axis by each sink S_i can be superimposed and give the total velocity vector $\vec{v}_a = \sum_{i=1}^{N} \vec{v}_{ai}$ shown in Fig. 4b. The sinks are considered in the middle of the elemental plume volumes [51, 52]. For a three-dimensional space, the velocity $\vec{v}_{ai}$ is calculated by the formula:

$$\vec{v}_{ai} = \frac{\delta\mu_1 \vec{s}_i}{4\pi s_i^3} \tag{5}$$

where $\vec{s}_i$ is a vector of the distance of point O_l from the sink S_i ($s_i = \mid \vec{s}_i \mid$). According to general practice, the volume strength is calculated by the continuity equation. However, for the present case of the annular plume, an analytical expression for the volume strength is utilised. Since the two plane plumes are identical, computations are performed in the one on the right and the results are valid for the whole annular-plume infinitesimal sectors. A potential flow velocity $\vec{v}_a$ with components u_a and w_a in the directions ψ and ξ, correspondingly, is calculated at the trajectory points of the plane plume at each level z (Fig. 4b). The velocity components are involved in the solution of the ordinary differential equations (ODE), which will be derived afterwards. In the present case, the velocity u_a is always negative for the plume on the right. Under the approximation explained above, Eqs. (1)–(4) describe the 2D plane plumes if $i = 0$ and the round plume if $i = 1$. For the plane plume on the right, the following boundary conditions must be satisfied:

$$\left.\begin{array}{l} u = 0, w = w_m + w_a, c = c_m, \tau_{\psi\xi} = 0, u'c' = 0, p_d \approx 0 \ \text{ on } \psi = 0; \\ u = -u_{B0} + u_a, w = w_a, c = 0, \tau_{\psi\xi} = 0, u'c' = 0, p_d = 0 \ \text{ on } \psi = B_{w0}; \\ u = u_a, w = w_a, c = 0, \tau_{\psi\xi} = 0, u'c' = 0, p_d = 0 \ \text{ on } \psi = -B_{w0}. \end{array}\right\} \tag{6}$$

For the equivalent round plume, the boundary conditions must be satisfied:

$$\left.\begin{array}{l} u = 0, w = w_m, c = c_m, \tau_{r\xi} = 0, u'c' = 0, p_d \approx 0 \ \text{ on } r = 0; \\ u = -u_{B1} + u_a, w = 0, c = 0, \tau_{r\xi} = 0, u'c' = 0, p_d = 0 \ \text{ on } r = B_{w1}; \end{array}\right\} \tag{7}$$

where u_{B1} is the entrainment velocity of the equivalent round plume; B_{w1} is the half width of the round plume, which is defined as $B_{w1} = n_{B1} b_{w1}$; $b_{w1} = K_{w1} z$; B_{w0} is the half width of the plane plume, which is defined as $B_{w0} = n_{B0} b_{w0}$; $b_{w0} = K_{w0} \xi$; for plane plumes $n_{B0} \cong 2$ and $K_{w0} = 0.132$ and for round plumes $n_{B1} \cong \sqrt{2}$ and $K_{w1} = 0.11$ are the spreading rate coefficients for the velocity field [43]; u_{B0} is the entrainment velocity of the inclined plane plume at the nominal external boundary. This velocity is calculated by solving the equivalent round plume and using the volume flux increment $\delta\mu_1$ divided by the infinitesimal surface of the round plume boundary $2\pi B_{w1}\delta z$ that corresponds to the z-cross-section. Thus, the velocity applied in the plane plume reads:

$$u_{B0} = \frac{\delta\mu_1/\delta z}{2\pi B_{w1}}. \tag{8}$$

Equation (8) replaces the continuity equation regarding the plane plume. It is also assumed that the transverse velocity and concentration profiles at a cross-section of the plane plume beyond the core region ($z > 7d_0 = 0.07$ m) may be approximated by the Gaussian-type profiles of the form:

$$\frac{f}{f_m} = \exp(-n^2) \tag{9}$$

which are valid from $n = 0$ to $n = n_{Bi}$, where f denotes either w or c; f_m denotes the centreline values either w_m or c_m; $n = \psi/b_{w0}$ for the plane plume and $n = r/b_{w1}$ for the round plume are the correspondingdimensionless distances from the plane plume trajectory and annular plume centreline. The corresponding half widths for the velocity and concentration field are b_{w0}, b_{w1} and $b_{c0} = \lambda_0 b_{w0}$ and $b_{c1} = \lambda_1 b_{w1}$, where λ_0 and λ_1 are the spreading rate ratios for concentration over the velocity. Note that the nominal widths are defined at the transverse distance ψ or r, where the axial velocity becomes equal to e^{-1} of the w_m or c_m.

3.3 Analytical expression for the strength of sinks

The strength $\delta\mu_1$ of the sink located at the level z of the annular plume centreline is considered equal to the volume contribution corresponding to the infinitesimal slice δz of the annular plume. Since the mean flow properties are well known regarding the round plume [43], it is straightforward to derive $\delta\mu_1$ through the volume flux $\mu_1 = \pi b_{w1}^2 w_m$, after differentiating with respect to z and substituting the centreline velocity for round plumes, $w_m = w_0 A_1 F_0^{-2/3}(z/d_{eq})^{-1/3}$. Then, after some manipulations, the following normalised relationship in dimensionless form is obtained:

$$\frac{\delta S}{\delta Z} = \sigma_1 Z^{2/3} \tag{10}$$

where $\delta S = (\delta\mu_1/\mu_{01})F_0^{-1}$, $A_1 = 3.71$, $\sigma_1 = \frac{20}{3}K_{w1}^2 A_1 = 0.3$. Equation (10) can be easily integrated from 0 to Z and the following relationship is derived:

$$\frac{S}{S_0} = 1 + \sigma_2 F_0 Z^{5/3} \tag{11}$$

where $S/S_0 = \mu_1/\mu_{01}$ is the bulk dilution; $S_0 = F_0^{-1}$; $\sigma_2 = \frac{3\sigma_1}{5} = 0.18$ and $\mu_{01} = \pi d_{eq}^2 w_0/4$ is the kinematic volume flux of the annular plume at the exit. The normalised variations of the strength $\delta S/\delta Z$ and dilution S/S_0 are shown in Fig. 5 with respect to the normalised vertical distance Z. Relationships (10) and (11) can be used for direct calculation of the strength of sinks and volume flux. The most important reason is the convergence of the procedure and the very good stability of computations in the core region of the annular plume. This is significant for getting results with a satisfactory accuracy from the early beginning of z, as the self-merging of the annular plume occurs very close to the plume exit.

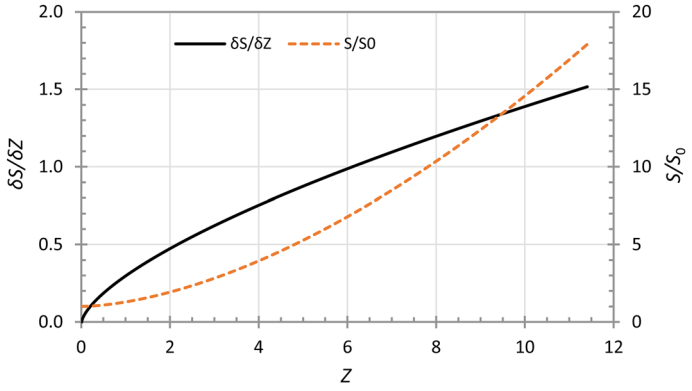

Fig. 5 Variation of the normalised strength of sinks $\delta S/\delta Z$ located at the centreline of the annular plume (solid line); and variation of the dilution S/S_0 (dashed line) for $F_0 = 1.63$, both as functions of the normalised centreline distance Z

3.4 The side-plane plume trajectory prediction

The trajectory of the plane plume, as forced by the flow potential, the entrainment from the external boundary, and the entrainment starvation at the internal boundary, can be predicted by SMA. SMA solves the integral equations of ξ- and ψ-momentum along with the tracer conservation equation under the approximations and assumptions described above. The complete forms of the integral equations are the ordinary differential equations (ODE):

ξ-momentum

$$\frac{\mathrm{d}m}{\mathrm{d}\xi} = \zeta \sin\theta - (u_B + u_{-B})w_a - u_a \mu \frac{\mathrm{d}\theta}{\mathrm{d}\xi}; \tag{12}$$

ψ-momentum

$$\frac{\mathrm{d}\theta}{\mathrm{d}\xi} = \frac{\zeta \cos\theta + (u_B + u_{-B})(u_B - u_{-B} - u_a) + n_{B0}K_{w0}w_a(u_B - u_{-B})}{m + 2w_a\mu + B_{w0}[2w_a^2 + (u_B + u_{-B})(u_B - u_{-B} + n_{B0}K_{w0}w_a)]}; \tag{13}$$

tracer conservation

$$\frac{\mathrm{d}\beta}{\mathrm{d}\xi} = -w_a \frac{\mathrm{d}\zeta}{\mathrm{d}\xi}; \tag{14}$$

where u_B and u_{-B} are the entrainment velocities at the boundaries on the right and left, correspondingly. Regarding the side-plane plume on the right, the outer entrainment velocity is $u_B = u_{B0}$, while the inner entrainment velocity is assumed $u_{-B} = 0$. For the solution of the vertical round plume, the final forms of ODE are:

continuity

$$\frac{\mathrm{d}\mu}{\mathrm{d}z} = 2\pi B_{w1} u_{B1}; \tag{15}$$

z-momentum

$$\frac{\mathrm{d}m}{\mathrm{d}z} = \zeta; \tag{16}$$

tracer conservation

$$\frac{\mathrm{d}\beta}{\mathrm{d}z} = 0; \tag{17}$$

where μ, m, ζ and β are the fluxes of volume, momentum, weight deficit and buoyancy, defined in Table 1. For the side plane plume, $\mathrm{d}\zeta/\mathrm{d}\xi = 0$, because $c_m = B_{p0}F_0^{2/3}(\xi/d_0)^{-1}$ [43], while for the equivalent round plume, $\mathrm{d}\zeta/\mathrm{d}z = -g_0'(\pi/3)\lambda_1 b_{w1}^2 c_m$, as derived from the related fluxes given in Table 1.

The self-merging trajectory of the annular plume has been measured experimentally and predicted by applying SMA. The alternative model SM could be also used to predict the self-merging of the annular plume, but this needs entirely different manipulations, which deviate from the present scope. SMA is a Fortran Power Station code prepared in the context of the present study. It solves the system of integral equations (12)–(17) along with the fluxes and their initial values given in Table 1. It utilizes the 4th order Runge–Kutta algorithm, and the results of the solution are direct. The solution proceeds as follows:

Iteration $k = 1$. Equations (15)–(17) for the round plume equivalent to the annular plume are solved for a prescribed marching step δz and initial conditions. The strength $\delta\mu_1$ of the sink, the volume flux μ_1, the mean axial velocity and mean concentration are determined at z. The strength $\delta\mu_1$ and the volume flux μ_1 are calculated by (10) and (11), correspondingly.

Iteration $k = 2$. Equations (12)–(14) for the plane plume on the right are initially solved with entrainment from the external boundary only and zero velocity components by the flow potential, $u_a = w_a = 0$. The entrainment velocity is taken equal to that of the equivalent round plume computed in previous iteration $k = 1$ and the plane plume trajectory is calculated. Using the same δz, the marching step for the plane plume is $\delta\xi = \delta z/\sin\theta$, where θ is the local inclination angle of the plane plume trajectory. Then, the values of u_a and w_a induced by all the sinks assigned along the round plume centreline, are calculated at the trajectory points of the plane plume defined by $\delta\xi$ steps.

Iterations $k = 3 - 4 - 5$. The computations are repeated for the side plane plume, considering for each iteration the renewed values of the trajectory inclination θ and the velocity components u_a, w_a from the previous iteration, due to slight changes of the plane plume

Table 1 Kinematic fluxes, their determination applying the Gaussian profiles (9) and their initial values at the source of area A_0, for a side plane plume ($i = 0$) and the equivalent round plume ($i = 1$)

Flux	Definition	Determination	Initial value
Volume	$\mu = \int_A w\,\mathrm{d}A$	$\mu = \left(\sqrt{\pi}b_{wi}\right)^{1+i} w_m$	$\mu_0 = A_0 w_0$
Momentum	$m = \int_A \left(w^2 + w'^2\right)\mathrm{d}A$	$m = \lambda_M\left(\sqrt{\frac{\pi}{2}}b_{wi}\right)^{1+i} w_m^2$	$m_0 = A_0 w_0^2$
Weight deficit	$\zeta = \int_A g'\,\mathrm{d}A$	$\zeta = g_0'(\sqrt{\pi}\lambda_i b_{wi})^{1+i} c_m$	$\zeta_0 = A_0 g_0'$
Buoyancy	$\beta = g_0' \int_A \left(cw + c'w'\right)\mathrm{d}A$	$\beta = \frac{\lambda_{Bi}}{\gamma_i} g_0'\left(\sqrt{\frac{\pi}{2}}\lambda_i b_{wi}\right)^{1+i} w_m c_m$	$\beta_0 = g_0'\mu_0$

trajectory, up to get the appropriate convergence. The effect of flow potential ceases for the trajectory points with $r_m \leq B_{w0} \sin\theta$, where r_m is the horizontal distance of the trajectory points from the z axis. This action is taken because the transverse velocity and concentration profiles of the two plane plumes at this distance start overlapping on each other. The profile overlapping may lead to erroneous reattachment location, since SMA does not take this effect into account.

4 Results and discussion

4.1 Core region of the annular plume

4.1.1 Trajectory prediction of the equivalent plane plume

Figure 6 depicts the trajectory of the side plane plume of the annular plume, as predicted by SMA in comparison with measurements. The complete convergence of the trajectory of the plane plume is obtained for $k = 3$ or up to 5. For instance, for the initial conditions $w_0 = 0.527$ m/s, $T_0 = 68.5$ °C, $T_a = 23$ °C for dry air, using $\delta\xi = 5 \times 10^{-5}$ m, which is the smallest step to get practically a limit independent of $\delta\xi$, the accuracy in millimeters is obtained at the 5th iteration. The limit obtained for a marching step equal to 10^{-4} m differs 1.0% of the above final limit. Using a desktop computer with processor Intel®Xeon®CPU X5650 2.67 GHz, RAM 12GB and 64bit operating system, the computational time needed for the solution of the equivalent round plume, with the smallest step, for 22,500 steps and then, calculating the side plane plume for 8 iteration cycles, is only 102.8 s. This is one of the best advantages of the integral method.

A linear interpolation of measurements with a coefficient of determination $R^2 = 0.8713$ is described by Eq. (18) shown with dotted line in Fig. 6.

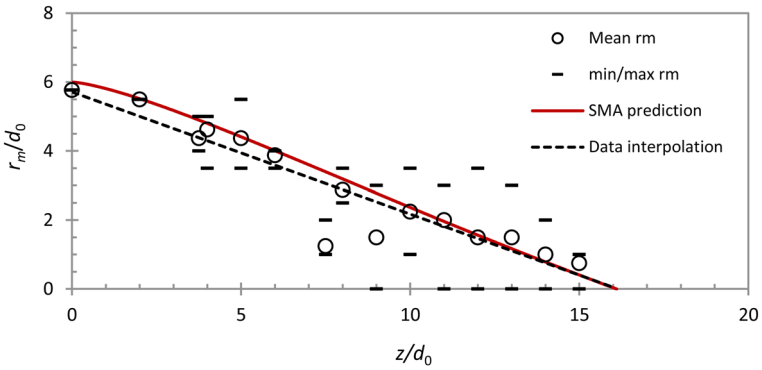

Fig. 6 Trajectory prediction of side plane plume of the annular plume by SMA (red solid line) in comparison to experimental data; open circles show the mean location of the trajectory measured at the axes $x, -x, y, -y$, which correspond to the maxima of velocities of upward direction, and bars show the min/max values; dotted black line is equation (18), which interpolates linearly the data given and intersects the annular-plume centreline at $z_{P0} = 16.1d_0$

$$r_m = r_{m0}\left(1 - \frac{z}{z_{P0}}\right) \tag{18}$$

where $r_{m0} = 5.71d_0$ and $z_{P0} = 16.1d_0$. The measurements represent the mean location of the trajectory at the four locations $x, -x, y, -y$ of each cross-section, as well as the min and max values. It is observed that they show appreciable scatter mainly for $z \geq 7d_0$, which will be explained below. The trajectory for the complete merging predicted by SMA is also shown in Fig. 6 in comparison to the experimental measurements. The accuracy obtained by SMA is very good, since the predicted trajectory agrees well with the measured mean location of the trajectory (open circles). The reattachment point P_0, where the trajectory intersects the centreline z-axis, as defined in Figs. 1 and 4, is predicted by SMA to be at $z = 16.0d_0$. This result is very close to the experimentally measured value.

4.1.2 Variation of the centreline velocities

The variation of the dimensionless mean axial velocity w_m/w_0, measured along the annular plume centreline dimensionless distance z/d_0 in the core region, is shown in Fig. 7. Two sets of measurements are shown: One set with mean exit velocity $w_0 = 0.527$ m/s, which includes the runs V1.1-1.6 with the statistical data of raw measurement values given in "Appendix 2" (Table 6), and another set with $w_0 = 0.702$ m/s that includes the run V1.7 with the statistical data of raw measurements given in "Appendix 2" (Table 7). Table 2 includes the locations and values of the characteristic quantities of the annular plume in the core region along with useful remarks. It is observed that the location of the minimum velocity (downward maximum velocity) has increased by 27.6% for a 33.2% initial velocity increase. This location of the core axis has the lowest total pressure. This means that it is at the neighbourhood level of the vortex centre. An increase of 33.2% of the initial

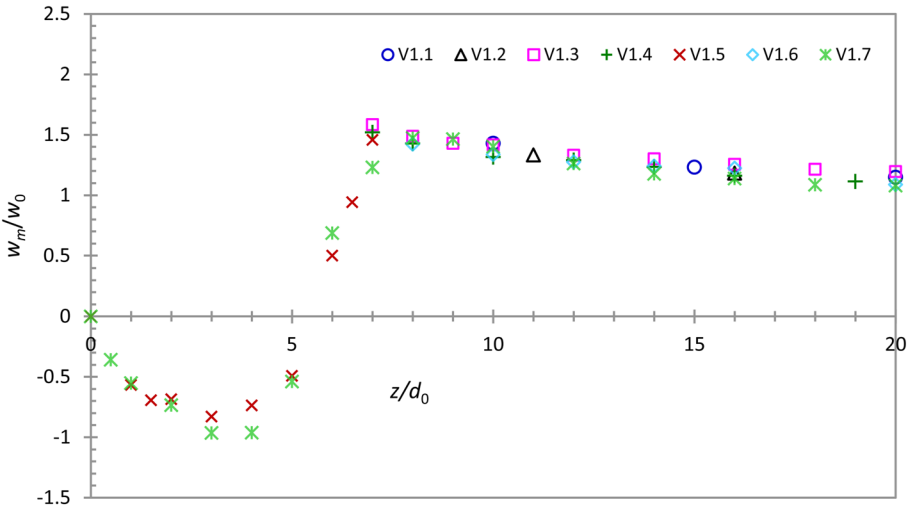

Fig. 7 Measured centreline variation of the dimensionless axial velocities w_m/w_0 of the annular plume in the core region with respect to the dimensionless distance z/d_0. The maximum velocity occurs at the point P_0' shown in Fig. 4b; the core region includes the vortex ring and the self-merging; symbol size is approximately equal to confidence interval for $a = 0.001$; runs V1.1-1.6 correspond to $w_0 = 0.527$ m/s and V1.7 to $w_0 = 0.702$ m/s

Table 2 Values of characteristic quantities of the annular plume in the core region

Description	Case with $w_0 = 0.527$ m/s	Case with $w_0 = 0.702$ m/s	Relative difference (%)
Location (z/d_0) of min w_m that corresponds to minimum total pressure	2.742	3.5	27.6
Minimum w_m/w_0	− 0.926	− 1.027	10.9
Stagnation point, z_{P1}/d_0	5.424	5.512	1.6
Location (z/d_0) of max w_m	7.0	8.35	19.3
Maximum w_m/w_0	1.521	1.480	− 2.7
w_m/w_0 at $z/d_0 = 16$	1.211	1.138	− 6.0

velocity caused a 10.9% increase of the absolute value of downward maximum velocity. Nevertheless, the location of the stagnation point P_1 remained practically unaffected by the variation of the initial velocity (1.6% upward shift). The location of the stagnation point was at $z_{P1} = 5.424d_0$, for the case of $w_0 = 0.527$ m/s, which is in good agreement with the experimentally observed location $z_{P1} \cong 5.5d_0$ obtained using a very thin nylon strip (see **movie1** along with the description in "Appendix 1"). The location of the maximum centreline velocity was shifted upwards by 19.3% for a 33.2% increase of the initial velocity, while the value of the maximum velocity remained practically unaffected (2.7% reduction only).

The internal recirculating region of the present case is found within the region $0 \le z < D_0/2$, in accordance with the experimental observations described by Chigier and Beer [53] and Ko and Chan [20]. Paying attention to Figs. 6 and 7, the results show that the locations of the reattachment point and the maximum centreline velocity do not coincide, as it happens in annular jets [19, 21, 53] and in a pair of identical slot jets [54], where one or two orders higher initial velocities were used than the velocities of the present work. Regarding the case with $w_0 = 0.527$ m/s, Fig. 6 indicates that the reattachment of the annular plume occurred at the longitudinal distance $z_{P0} = 16.1d_0$, which contradicts the result shown in Fig. 7, where the maximum centreline velocity occurred at the considerably shorter distance of $7d_0$ (point P_0' in Fig. 4b). Careful and scrutinised observation of the phenomenon and the measurements depicted in Fig. 8 in contrast to Figs. 6 and 7 explains the above difference and proves that the correct reattachment location is the centreline distance $z_{P0} = 16.1d_0$. This decision is based on the following reasoning:

As shown in Fig. 8, the pink and white coloured regions represent the regions where w/w_m is approaching or being equal to 1. These regions are observed at remote radial distances for $z/d_0 = 3.75$ and 5 (Fig. 8a, b), while they are gradually approaching each other for $z/d_0 = 7.5$ and 15, although they remain distinct (Fig. 8c, d). This means that reattachment has not occurred yet. These regions are observed unified in a restricted area for $z/d_0 = 30$ (Fig. 8e). Therefore, it is concluded that the reattachment occurs beyond the longitudinal distance $z/d_0 = 15$, which agrees with the measurements shown in Fig. 6, where the reattachment occurs at $z/d_0 = 16.1$. The four pink areas read weird in Fig. 8a, b, because of measuring at locations $(|x|, 0, z)$, $(-|x|, 0, z)$, $(0, |y|, z)$ and $(0, -|y|, z)$ only. Thus, it is implied that the above differences are owed to the low initial momentum compared to buoyancy ($F_0 < 2$) and the vortex ring induced in the region $0 \le z/d_0 < 5.5$. Such a buoyant flow presents instabilities and the velocity trajectories of the annular plume along with the reattachment point P_0 oscillate and flicker

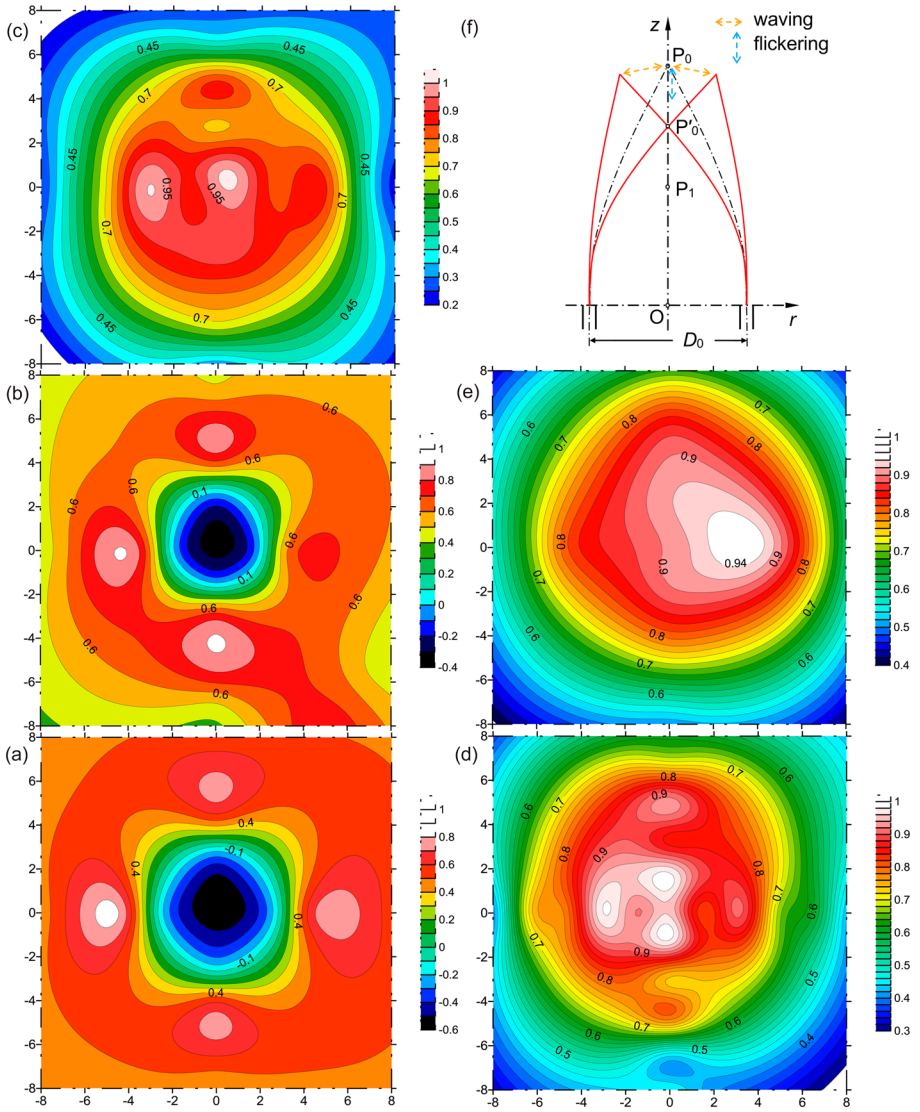

Fig. 8 Isovelocity contours of the velocity ratio w/w_m of the annular plume at the cross-sections z/d_0: **a** 3.75; **b** 5; **c** 7.5; **d** 15 and **e** 30; drawing **f** shows schematically the unstable core trajectories of the annular plume. The initial velocity was $w_0 = 0.527$ m/s and the measurements were performed at several radial distances on the perpendicular axes x and y of each cross-section

like a candle flame, as schematically shown in Fig. 8f. It is noted that a plane jet attaching to an offset parallel wall is oscillating due to the infinitesimal periodic pressure fluctuations [55]. Unlike the plane jet, the most possible reasons that an annular plume is oscillating are the low momentum compared to buoyancy in conjunction with flow and temperature asymmetries induced by the vortex ring. Thus, the sensor placed at P_0

measured the centreline axial velocity with considerable fluctuations. On the contrary, the same sensor placed at P_0', between the stagnation point P_1 and the point P_0, where the axial velocities present restricted scatter compared to axisymmetric values (see also Figs. 6, 7 and 8a, b), measured the centreline maximum velocity.

For initial velocity $w_0 = 0.527$ m/s, the centreline values of maximum velocities measured in the region $z/d_0 = 7$ to 8 are about 20% higher than the corresponding values measured at $z/d_0 = 16.1$. Increasing the initial velocity, the location of the maximum velocity is shifted and approaches more and more to P_0, due to succeeding rather better stability conditions. An upward shift of the reattachment point occurs as well. To explain if this shift happened for $w_0 = 0.702$ m/s, axial velocity measurements at several radial distances along x and y axes of the cross-sections $z/d_0 = 16, 18, 20$ and 22 were made. The results are presented in isovelocity diagrams (Fig. 9a–d). It is evident from the diagrams that the most contracted 0.90-, 0.95- and 0.99-isovelocity contours happened in the cross-section $z/d_0 = 18$ (Fig. 9b), while the cross-section $z/d_0 = 20$ (Fig. 9c) is second in hierarchical order regarding shrinkage. However, the cross-section $z/d_0 = 18$ shows two separate 0.95-isovelocity contours in contrast to the cross-section $z/d_0 = 20$, where the velocity peak is found within the area circled by 0.99-isovelocity contour. It is noted that a similar event is observed little before the reattachment with $w_0 = 0.527$ m/s (Fig. 8d). Thus, it may be concluded that reattachment of the

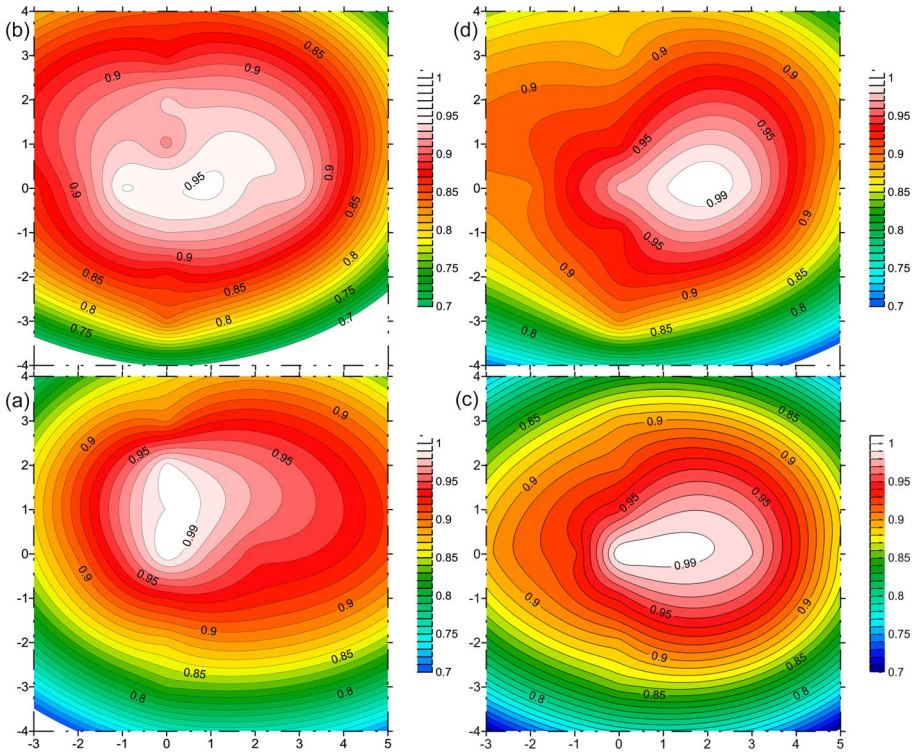

Fig. 9 Isovelocity contours of the velocity ratio w/w_m of the annular plume at the cross-sections z/d_0: **a** 16; **b** 18; **c** 20 and **d** 22. The initial velocity was $w_0 = 0.702$ m/s and the measurements were performed at several radial distances on the perpendicular axes x and y of each cross-section

annular plume occurs at $z/d_0 \cong 20$. SMA predicts it at $z/d_0 = 20.7$, which is very close to that detected. Ko and Chan [20] have correlated the position of reattachment with the dimensionless parameter $F_{m0} = \rho_a m_0/(A_{in}P_a)$, where m_0 is the initial kinematic momentum flux, A_{in} is the area included by the internal diameter of the annulus, and P_a is the atmospheric pressure in the internal region of the annulus near the closed bottom.

The static pressure (total pressure) at the centre of the vortex ring of either an annular jet [20] or a pair of parallel plane jets [54], is lower than the pressure at other core regions and directly affects the centreline point of the horizontal symmetry plane of the vortex ring, where the downward velocity is also maximised. Since pressure is correlated with initial momentum, an analogous result is expected to occur in annular plumes. Thus, the vortex centre will be at about the same level with the maximum value of downward centreline velocity, that is at $z_{vc}/d_0 = 2.742$ for $w_0 = 0.527$ m/s and at $z_{vc}/d_0 = 3.5$ for $w_0 = 0.702$ m/s. The experimental measurements of the present work concerning annular plumes showed that the vertical location of the vortex centre, z_{vc}, increases with the increase in the initial velocity and, consequently, with initial momentum, contrary to what takes place in annular jets [20]. The differences may be explained by considering that only momentum dominates the behaviour of annular jets, while the behaviour of annular plumes is rather dominated by buoyancy than momentum. Regarding annular jets, the higher the initial momentum, the higher the pressure drop, the more the contraction, and the more the shrinkage of the vertical location of the vortex ring. Regarding annular plume, the low values of Froude number indicate initially low momentum values, while the flow is accelerating due to initially high buoyancy and this effect contributes to a momentum increase. Therefore, the lower pressure occurs somewhat downstream than the case without flow acceleration; the centre of the vortex ring follows the same behaviour.

Careful observation of the isovelocity diagrams (Fig. 8) detects that the black coloured region of negative velocities in diagram Fig. 8a ($z/d_0 = 3.75$) is more contracted than that in Fig. 8b ($z/d_0 = 5$). This is expected since cross-section Fig. 8a is closer to the region of lower pressures than cross-section Fig. 8b. This is a very useful observation and it could be implemented as an indirect method of pressure estimation in plumes, where the total pressure is very small and not easily measurable. It is noted that a contraction also occurs immediately above the source of a lazy plume [56], which may be attributed to a pressure drop. The radial distance of the vortex ring is independent of the dimensionless pressure F_{m0} and, according to Ko and Chan [20], it is roughly at $r_{vc}/D_{out} \cong 0.18$. The upper level of the vortex ring should be a little below the observed location of the stagnation point (Table 2).

4.1.3 Important characteristics

Ko and Chan [20] have successfully correlated the locations of the reattachment point, the vortex centre and the stagnation point with the dimensionless pressure F_{m0}. This pressure is responsible for the outer entrainment in this region [20]. As shown in Fig. 10, the variation of F_{m0} may be divided in three regions: The low-pressure region ($F_{m0} < 0.1$), the intermediate-pressure region ($0.1 \le F_{m0} \le 3$) and the high-pressure region ($F_{m0} > 3$). It is evident that for $F_{m0} > 3$, the dimensionless location of the reattachment point, z_{P0}/D_{out}, is highly dependent on F_{m0}, while for $F_{m0} < 3$, this dependence is weak, and, for $F_{m0} < 0.1$, z_{P0}/D_{out} may depend on other parameters, like the buoyancy flux or the Froude number, as in the present cases of annular plumes. In the following the above locations are presented in relation to F_{m0}.

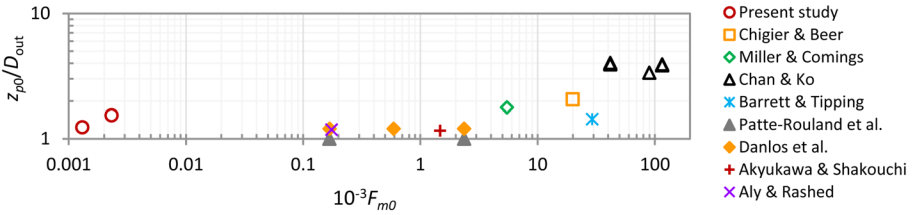

Fig. 10 Dimensionless reattachment point z_{P0}/D_{out} of the present experiments (red open circles) in correlation to the dimensionless pressure F_{m0}, regarding annular plumes with initial velocities $w_0 = 0.527$ and 0.702 m/s, compared to measurements available in the literature concerning annular jets with initial velocities in the range from 8 to 50 m/s

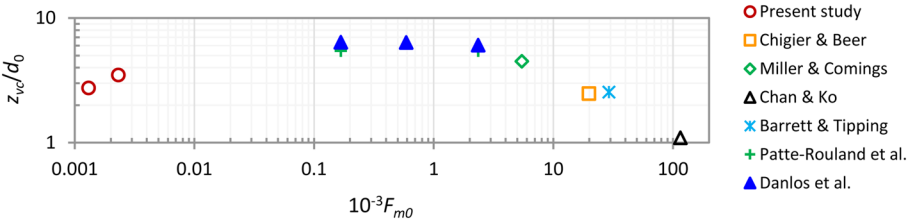

Fig. 11 Vertical dimensionless distance z_{vc}/d_0 of the vortex centre from the exit (red open circles) based on the location, where the downward velocity on the symmetry axis gets its maximum value, in comparison to the experimental values available in the literature; the values of z_{vc}/d_0 are correlated with the dimensionless pressure F_{m0}

Regarding the vertical location of the vortex centre, the results of experimental values found in the literature are depicted in Fig. 11 along with the corresponding observations of the present study for comparison. In this figure, the vertical location of the vortex centre z_{vc} is normalised by the exit width d_0 of the annulus, because in this manner a better presentation of the correlation is managed. For the correlation of z_{vc}/d_0 with F_{m0}, the three regions defined above are considered. In the high-pressure region, the experimental measurements show that the higher the momentum, the higher the absolute value of the pressure (pressure drop) prevailing in the core region near the closed bottom of the annulus. The higher the absolute pressure, the more intense the outer entrainment, and the shorter the distance from the source of the vortex centre. In the intermediate-pressure region, the vortex centre location seems to be rather independent of momentum, whereas in the low momentum region, the vortex centre distance from the exit increases with pressure increase, that is, increase of momentum or decrease of A_{in}.

Regarding the dimensionless location of the stagnation point, z_{P1}/d_0, a similar diagram to Fig. 11 is shown in Fig. 12, where z_{P1}/d_0 is correlated to F_{m0}. Paying attention to Fig. 12, a similar conclusion can be drawn as discussed previously for the distance of the vortex centre from the exit, with the difference that, for the low-pressure region, the stagnation point location is practically independent of F_{m0}. It is noted that, regarding the case of initial velocity $w_0 = 0.527$ m/s, the measurement reliability of the stagnation point location by the transducer has been visually verified using the video **movie1** provided in "Appendix 1". Unfortunately, no experimental studies were found in the literature concerning annular plumes with low values of F_{m0} to compare them with the corresponding

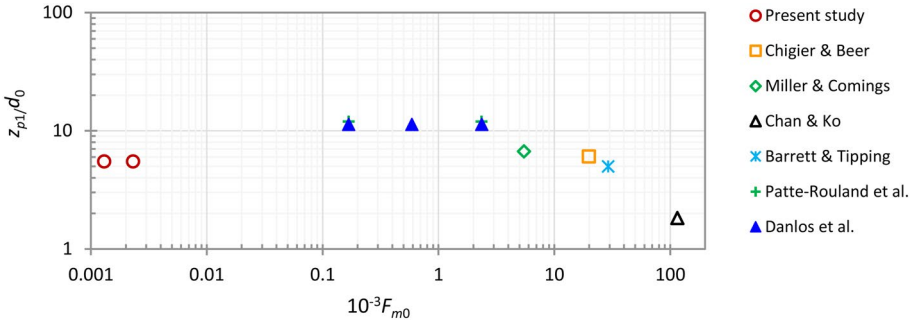

Fig. 12 Vertical dimensionless distance of the stagnation point z_{p1}/d_0 based on the observed and measured locations (red open circles), where the velocity on the symmetry axis changes direction from upward to downward, in comparison to the measurements available in the literature; the values of z_{p1}/d_0 are correlated with the dimensionless pressure F_{m0}

results of the present work. The only relevant work found is the computational study by Wang et al. [27], which has investigated the diameter ratios $D_{out}/D_{in} = 5/4, 5/3, 5/2$ and 5/1 of an annular plume with initial velocity $w_0 = 1.2$ m/s and air temperature 95 °C at the source exit, as well as other combinations of the initial velocity with higher temperatures. For the case $D_{out}/D_{in} = 5/4 = 1.25$, which resembles the experiments of the present work, where $D_{out}/D_{in} = 1.181$ and SMA is valid, Wang et al. [27] have computed the location of the reattachment point at the axial distance $z/D_{out} = 2.6$. SMA predicts this location at $z/D_{out} = 1.275$.

4.1.4 A new correlation of the reattachment location

Based on the overall information given above, it is possible to apply DA to correlate the location of the reattachment point, z_{P0}, with the initial kinematic momentum m_0, the annular source area A_0, a buoyancy parameter like the effective gravitational acceleration, g'_0, and the annulus diameter ratio, D_{out}/D_{in}. The above dimensional independent variables include two dimensions and, thus, they can form only two dimensionless independent variables by their suitable combination. These variables may be the initial Froude number F_0 and the annulus diameter ratio D_{out}/D_{in}. After pertinent manipulations, the normalised reattachment distance, $Z_{P0} = (z_{P0}/d_{eq})F_0^{-1}$ is correlated to the normalised dimensionless independent variable $(D_{out}/D_{in})F_0^{-1/3}$. Due to the lack of available measurements in the literature, the two cases measured in the present study are used, regarding z_{P0} values along with computed values for other cases in the region where SMA is valid; these values are given in Table 3. Data show that Z_{P0} is slightly dependent on $(D_{out}/D_{in})F_0^{-1/3}$; thus, it may be considered as practically independent.

The horizontal dashed line in Fig. 13 represents the mean value of the computed values also depicted for the initial velocities $w_0 = 0.527$, 0.702 and 1.054 m/s. It is shown that the measured values of the reattachment point locations for the initial velocities $w_0 = 0.527$ and 0.702 m/s lie very close to the mean value of the data. Therefore, for annular plumes, a simple relationship is derived for the location of the reattachment point:

Table 3 Input and output values of parameters of SMA for the predicted cases plotted in Fig. 13

D_{out} (m)	0.13	0.13	0.13	0.13	0.13	0.13	0.13
D_{in} (m)	0.128	0.12	0.11	0.096	0.085	0.074	0.065
d_{eq} (m)	0.02272	0.05000	0.06928	0.08766	0.09836	0.10688	0.11258
Run	1	2	3	4	5	6	7
w_0 (m/s)	0.527	0.527	0.527	0.527	0.527	0.527	0.527
g_0' (m/s^2)	1.5072	1.5072	1.5072	1.5072	1.5072	1.5072	1.5072
F_0	2.85	1.92	1.63	1.45	1.37	1.31	1.28
z_{P0}	0.079	0.135	0.161	0.181	0.190	0.197	0.202
Run	8	9	10	11	12	13	14
w_0 (m/s)	0.702	0.702	0.702	0.702	0.702	0.702	0.702
g_0' (m/s^2)	1.5783	1.5783	1.5783	1.5783	1.5783	1.5783	1.5783
F_0	3.71	2.50	2.12	1.89	1.78	1.71	1.67
z_{P0}	0.115	0.177	0.208	0.231	0.242	0.251	0.256
Run	15	16	17	18	19	20	21
w_0 (m/s)	1.054	1.054	1.054	1.054	1.054	1.054	1.054
g_0' (m/s^2)	1.5072	1.5072	1.5072	1.5072	1.5072	1.5072	1.5072
F_0	5.70	3.84	3.26	2.90	2.74	2.63	2.56
z_{P0}	0.183	0.266	0.309	0.342	0.359	0.371	0.378

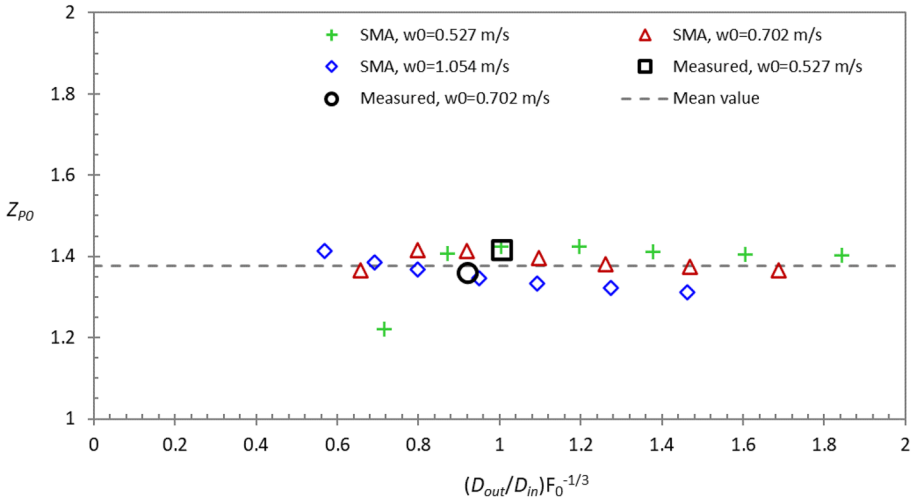

Fig. 13 Normalised dimensionless distance Z_{P0} of reattachment point of annular plume correlated with the dimensionless quantity $(D_{out}/D_{in})F_0^{-1/3}$; black symbols represent the measured values, while green, blue and red symbols the calculated values using SMA

$$Z_{P0} = \frac{z_{P0}}{d_{eq}} F_0^{-1} = 1.38 \pm 0.05 \tag{19}$$

Equation (19) is valid for $d_0/D_0 \leq O(0.1)$, which is approximately equivalent to the region $1 < D_{out}/D_{in} \leq 2$. This region agrees with that estimated by applying the method of conformal mapping described in "Appendix 3". The result obtained indicates that the dimensionless reattachment distance depends mainly upon the initial Froude number and the equivalent diameter of the annular plume.

4.1.5 Trajectory of maximum temperatures or concentrations

The trajectory of the maximum relative temperatures or concentrations measured along the annular plume in the core region is shown in Fig. 14a. The statistical data of raw measurement values, where the values of dimensionless quantities of Fig. 14 are based on, are given in "Appendix 2" (Table 10). The black open symbols (rhombus) represent the locations of measurements along the annular plume centreline, which shows some eccentricity with respect to centreline due to asymmetries originating probably from the vortex ring and low momentum. The red open circles represent the locations of the maximum values measured at the corresponding cross-sections. The red and black symbols are measurements with 32 to 33 °C of background temperature, while the blue triangles are measurements with 20 °C of background temperature. It is shown that the trajectory defined by the maximum relative temperatures or concentrations intersects the centreline at $z/d_0 \cong 6$,

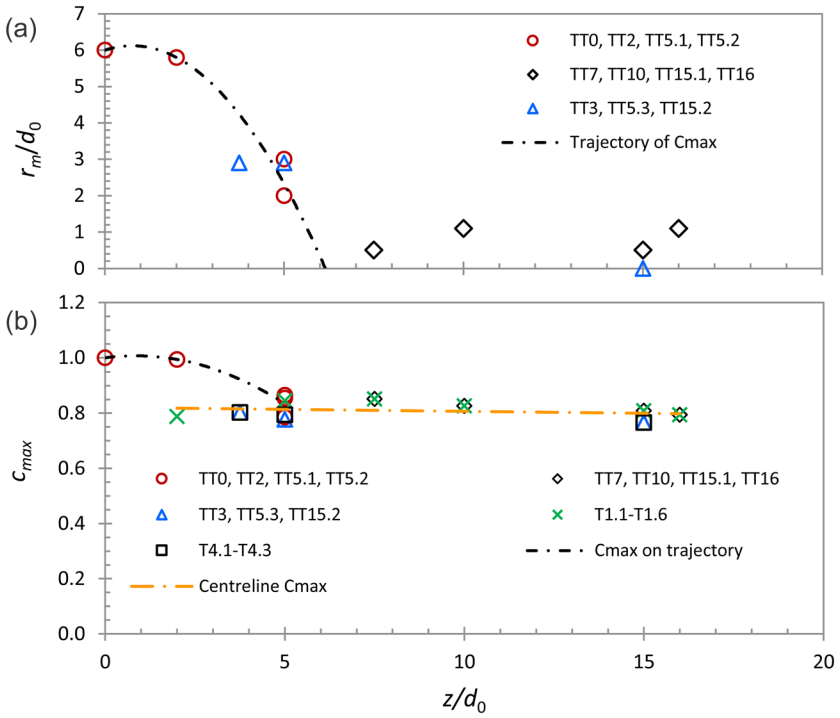

Fig. 14 **a** Measured trajectory of dimensionless maximum temperatures or concentrations; and **b** maximum and centreline values of concentrations, with respect to the dimensionless distance z/d_0 (red open circles, black open rhombus and blue open triangles); the symbol size is approximately equal to the confidence interval for $a = 0.001$

which is a very short distance from the annular source exit and within the vortex ring area. This is a result of the vortex ring, which recirculates part of the exit hot air to the plume centreline and then downward up to the bottom of the internal core region. Consequently, the centreline air temperatures become high enough, approaching the ring exit values, as this is shown in Fig. 14b. This figure also shows that the centreline concentrations and subsequently the temperatures remain approximately at the same level along the core (2 °C temperature decay from $z/d_0 = 5$ and up to 16).

Another noteworthy observation is that the trajectory of the relative maximum temperatures or concentrations presents a steeper inclination towards the symmetry axis z than the corresponding for the maximum velocities shown in Fig. 6, effectively suppressing the nonuniformity of the temperature field within the core region. Additional measurements of temperature at the locations $(r/d_0, z/d_0)$ $(0, -0.3)$ and $(5.0, -0.3)$ at the bottom of the internal region, using the HH147 Omega thermometer, recorded mean temperatures of 53.4 °C and 54.4 °C, respectively, which correspond to the concentrations $c = 0.691$ and 0.712, for $F_0 = 1.86$. These values are within the range of the values measured in the core region. The physical interpretation of this finding is attributed to the recirculation of a part of the exit hot air by the vortex ring. The equivalent round plume to the annular plume has a source and core region of shorter dimensions without a vortex ring. Thus, the dilutions in the core region of the annular plume become higher than those of the round plume at the same axial distance.

4.2 Near field beyond the core region

4.2.1 Centreline velocity variation

The variation of the mean axial velocity along the centreline of the annular plume is predicted by SMA. Furthermore, the following analytical relationship (20) [48], which is based on the superposition of kinetic energy fluxes, if the source of the equivalent round plume is considered that consists of point sources, is shown in Fig. 15 in comparison to experimental data.

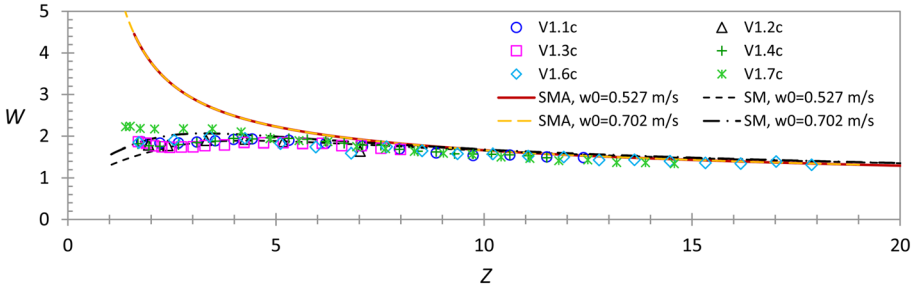

Fig. 15 Variation of the normalised axial velocities $W = (w_m/w_0)F_0$ along the centreline of annular plume with respect to the normalised distance $Z = (z/d_{eq})F_0^{-1}$. The experimental measurements (symbols) are compared to SMA and SM predictions; the symbol size is approximately equal to the confidence interval for $a = 0.001$

$$W = A_1 Z^{-1/3}\left[\frac{4}{3}\left(\frac{b_{w1}}{d_{eq}}\right)^2\left\{1-\exp\left[-\frac{3}{4}\left(\frac{b_{w1}}{d_{eq}}\right)^{-2}\right]\right\}\right]^{1/3} \tag{20}$$

where $W = (w_m/w_0)F_0$. The centreline velocity measurements, where W and Z are based on, are given in "Appendix 2" (Tables 11 and 12). The variation of the normalised mean axial velocity W along the annular plume centreline calculated by SMA and by SM is shown in Fig. 15.

The runs V1.1c-V1.6c concern the annular plume with initial velocity $w_0 = 0.527$ m/s, while V1.7c concerns the annular plume with $w_0 = 0.702$ m/s. It is evident that the effect of nozzle geometry maintains in the core region up to $Z \cong 5$. Beyond this distance, the annular plume behaves like a round plume having an equivalent diameter d_{eq}. Neither SMA nor SM can predict the centreline velocities in the reverse flow region occupied by the vortex ring. SMA significantly overestimates the centreline velocities in the region $Z < 4$ corresponding to $z < 49d_0$, which is affected by the core region instabilities, as explained previously. Contrary to SMA, exempting the region $0 < Z < 2$, where SM underestimates the velocity, for $Z \geq 2$ SM shows good agreement with the measurements. SMA predictions are significantly improved for $Z > 5$, where both model predictions are practically in agreement.

4.2.2 Centreline temperature or concentration variation

The variation of the mean relative temperature or mean concentration along the centreline of the annular plume is predicted by SMA. Figure 16 shows the centreline variation of the normalised mean concentrations $C = (c_m/c_0)F_0$ with respect to the normalised centreline distance Z. Open circles represent the normalised mean concentrations calculated by the temperature measurements given in "Appendix 2" (Table 13). The red solid line is SMA prediction regarding the equivalent round plume of the annular plume. This

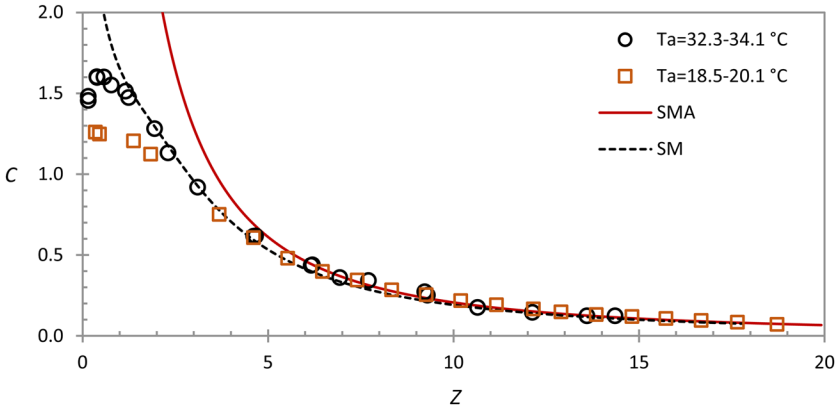

Fig. 16 Variation of the normalised mean concentrations $C = (c_m/c_0)F_0$ along the centreline of annular plume with respect to the normalised distance $Z = (z/d_{eq})F_0^{-1}$ for the case with $w_0 = 0.527$ m/s. Circles and squares show the experimental measurements; red solid line is SMA prediction and black dotted line is SM prediction; the size of symbols includes the interval limits for $a = 0.001$

method predicts very well the experimental results for $Z \geq 4$, when the velocity and temperature or concentration profiles tend to become Gaussian. For $Z < 4$, SMA prediction overestimates significantly the experimental data.

If the source of the equivalent round plume is considered as composed by point sources, after applying SM by superposing the buoyancy fluxes of all point plumes, the following relationship is taken for the plume centreline [47]:

$$\overline{WC} = \frac{\pi}{4}\lambda_{B1}^{-1}F_0^2\left[\mathrm{erf}\left(\frac{d_{eq}(1+\lambda_1^2)^{1/2}}{2\lambda_1 b_{w1}}\right)\right]^2 \tag{21}$$

where $\lambda_{B1} \approx 1.15$, $\lambda_{p1} \approx 1.04$, with the buoyancy flux expressed in the normalised form, $\overline{WC} = \overline{wc}/(w_0 c_0)F_0^2$. If equation (21) is divided by equation (20) for the centreline mean axial velocity, the analytical relationship for the mean centreline concentrations is derived:

$$C = \frac{\overline{WC}}{W} \tag{22}$$

The variation of the normalised concentration along the centreline, expressed by equation (22) is shown in Fig. 16 in comparison to the experimental measurements and SMA prediction. In contrary to SMA prediction, SM predicts excellently almost all the region, exempting only the region $Z < 2$, where the experimental data is overestimated. As shown in Figs. 15 and 16, the annular plume after complete merging obtains the behaviour of the equivalent round plume, regarding the centreline mean axial velocities and mean concentrations. A similar observation can be deduced for the centreline dilution, which is defined as $S_m = 1/c_m$. Comparing the centreline dilutions achieved in the region beyond the core of the annular plume ($Z > 5$), the annulus-type diffuser, which is equivalent to a rosette-type diffuser, attains equal dilutions to the rosette-type diffuser and the equivalent round plume with equal flow rates. Comparing the centreline dilutions achieved in the core region of the annular plume ($0 \leq Z \leq 1.6$) with the bulk dilutions achieved by a single round plume at the same centreline distances from the plume exit [38, 43], it is concluded that the annular plume succeeds 15 times on average higher centreline dilutions than the corresponding bulk dilutions of the round plume. These high dilutions may be attributed to the existence of the vortex ring, the outer entrainment increase due to the pressure drop inside the core and the longer mean diameter of the ring exit. Therefore, the annular plumes seem very promising for wastewater disposal in shallow water bodies.

4.3 Sensitivity analysis

4.3.1 Effect of strength of sinks

Figure 17 shows the significant differences between the values of $\delta\mu/\mu_0$ and μ/μ_0 calculated by the new relationships (10) and (11), and the corresponding values calculated by the continuity equation (15); $\mu_0 = 1986\,\mathrm{cm}^3/\mathrm{s}$. Figure 17a shows that the strength $\delta\mu$ calculated by (10) starts from a zero value and infinite derivative value at the plume exit and proceeds with gradually increasing values tending to infinity and decreasing derivative values tending to zero at infinity. The strength calculated by the continuity equation again starts from a zero value, but then increases abruptly and proceeds with gradually increasing values approaching the previous strength behaviour at infinity. The volume flux μ calculated

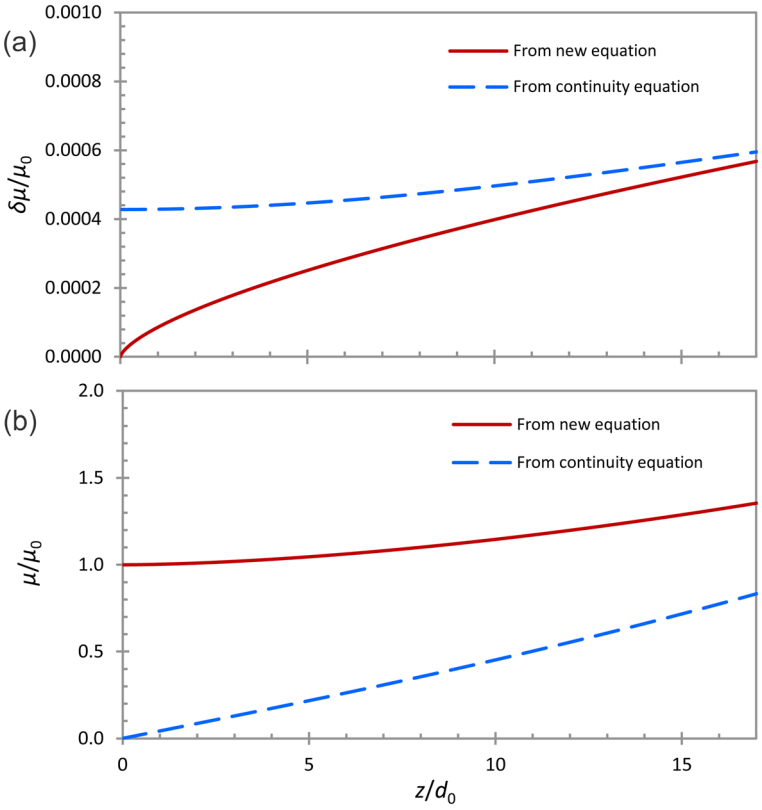

Fig. 17 Variation of the dimensionless **a** strength of sinks $\delta\mu/\mu_0$, and **b** dilution μ/μ_0, with respect to the dimensionless centreline distance z/d_0, for $w_0 = 0.527$ m/s and $F_0 = 1.63$. Comparisons between corresponding values calculated by the new relationships (10) and (11) (solid lines) and values computed by the continuity equation (dashed lines) of the equivalent round plume to the annular plume

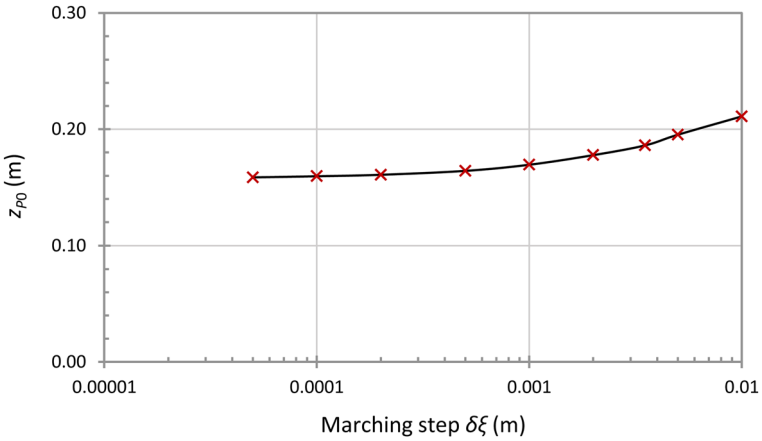

Fig. 18 Variation of the limits of convergence of SMA, regarding the reattachment distance z_{P0}, using strength of sinks and dilution values calculated by relationships (10) and (11) for $w_0 = 0.527$ m/s and $F_0 = 1.63$; the final limit is $z_{P0} = 0.16$ m obtained for $\delta\xi = 0.00005$ m and sinks in a 3D space

by (11) starts from μ_0 and a zero value of the derivative at the exit and proceeds with gradually increasing values tending to infinity. On the contrary, Fig. 17b shows that the volume flux μ calculated by the continuity equation starts from a zero value and a higher derivative value than the previous one and proceeds with gradually increasing values approaching the behaviour of the previous volume flux at infinity. The case of calculating the strength of sinks and the volume flux by the continuity equation constitutes the reason that the solution crashes even if under-relaxation is applied. Instead, the use of relationships (10) and (11) ensures an excellent, smooth convergence at the correct limit $z_{P0} = 0.16$ m, as shown in Fig. 18. The physical realism of the model and its ability to accurately predict laboratory measurements constitute additional factors to this excellent convergence. The numerical results by SMA indicated that the contribution of the flow potential to the self-merging of the annular plume is very small (only 1%), while the main contribution (99%) is owed to the outer entrainment combined with inner entrainment starvation.

4.3.2 Effect of relative humidity on model predictions

Using the perfect gas law, the thermal volume expansion of air is $\beta = T_a^{-1}$ (K^{-1}). This relationship is practically satisfactory for conditions of the standard atmosphere ($p = 101325$ Pa, $T_a = 288.15$ K)) and for adiabatically temperature variation of dry air volume with height in the troposphere. For these conditions, the website (last accessed on July 28, 2023) provided by NASA [57] is used to calculate the air densities with 6-digit accuracy. In such conditions the effective gravitational acceleration defined either through temperatures or densities results in almost the same value, as the following equation is valid:

$$g_0' = g\frac{T_0 - T_a}{T_a} \cong g\frac{\rho_a - \rho_0}{\rho_0} \tag{23}$$

Using (23), β can be well defined through the relationship:

$$\beta \cong \frac{\rho_a - \rho_0}{\rho_0(T_0 - T_a)} \tag{24}$$

Equations (23) and (24) are invalid for wet air conditions, because the moisture contained in the air affects the air density, which depends also upon the relative humidity (*RH*). According to EEL meteorological station, in the room of experiments, the *RH* varied from 40 to 65% during the measurement periods. It is interesting to estimate the relative errors made in model predictions regarding trajectory of self-merging, centreline axial velocities and concentrations for dry air conditions instead of the wet air conditions occurring during the experiments:

Let average $RH = 55\%$, average room temperature $T_a = 23$ °C, ring exit temperature $T_0 = 68.5$ °C and room altitude $H = 73$ m above sea level. For wet air conditions, the website (last accessed on July 28, 2023) provided by BARANI DESIGN Technologies s.r.o. [58] is used, which provides a density calculator, calculating the density with 4 digit accuracy as a function of air temperature, air relative humidity and barometric pressure or, alternatively, altitude above sea level. The corresponding air densities for air conditions given above are $\rho_a = 1.175\,\mathrm{kg/m^3}$ and $\rho_0 = 0.962\,\mathrm{kg/m^3}$, which give $g_0' = g(\rho_a - \rho_0)/\rho_0 = 2.172\,\mathrm{m/s^2}$. The corresponding density values for dry air conditions are $\rho_a = 1.18353\,\mathrm{kg/m^3}$ and $\rho_0 = 1.02569\,\mathrm{kg/m^3}$; thus $g_0' = 1.50963\,\mathrm{m/s^2}$, while

Table 4 Relative errors of predictions using dry air conditions instead of wet air conditions

Variable	Air condition	SMA	SM
z_{P0} (m)	$RH = 0\%$	0.160	Not applicable
	$RH = 55\%$	0.132	Not applicable
Relative error (%)		− 21.2	Not applicable
w_m (m/s) at $z = 60d_0$	$RH = 0\%$	0.7007	0.5832
	$RH = 55\%$	0.7755	0.6584
Relative error (%)		9.6	11.4
c_m at $z = 60d_0$	$RH = 0\%$	0.3423	0.2997
	$RH = 55\%$	0.3105	0.2655
Relative error (%)		− 10.2	− 12.9

Table 5 Relative errors of predictions using dry air conditions against measured values

Variable	Measured value	SMA	SM
z_{P0} (m)	0.161	0.160	Not applicable
Relative error (%)		0.6%	Not applicable
w_m (m/s) at $z = 60d_0$	0.611	0.701	0.583
Relative error (%)		− 14.7%	4.6%
c_m at $z = 60d_0$	0.315	0.342	0.300
Relative error (%)		− 8.6%	4.8%

$g_0' = 1.50719\,\mathrm{m/s^2}$, based on temperatures. Therefore, the mean effect on the Froude numbers ratio (dry F_{0d} over wet F_{0w}) regarding predictions is $F_{0d}/F_{0w} = 1.2$.

Using the dry air conditions instead of the wet air conditions given above, the model predictions and estimated relative errors are shown in Table 4. The relative error using dry air conditions instead of wet ones for SMA predictions of the reattachment point P_0 is − 21.2%. For the centreline mean velocity predictions at $z = 60d_0$, the relative errors are 9.6% and 11.4%, and for the concentrations − 10.2% and − 12.9%, regarding SMA and SM, correspondingly. The relative errors of model predictions for dry air conditions against the measured values are given in Table 5. The relative error for the reattachment point is 0.6% regarding SMA. The corresponding errors for the centreline mean velocities at $z = 60d_0$ are − 14.7% and 4.6%, while for the mean concentrations − 8.6% and 4.8%, regarding SMA and SM.

5 Summary and conclusions

The present study concerns the experimental, theoretical, and numerical investigation of the mean flow and mixing properties of a thermal annular plume in the core region and beyond it in the near field. Two sets of experimental runs were performed. One complete set with a flow rate of $1986\,\mathrm{cm^3/s}$ and another one with a flow rate of $2646\,\mathrm{cm^3/s}$ for only axial velocity measurements. The air velocity transducer TSI 8465 was used for velocity

measurements along with thin nylon strips to detect the velocity direction. A series of 14 thermocouples was used for temperature measurements.

In the core region, experiments on annular plumes with initial velocities $w_0 = 0.527$ and 0.702 m/s were performed. The mean flow and mixing characteristics at the areas along the trajectory of maximum values and along the centreline of the core were measured and predicted where possible. A vortex ring, the self-merger, the points of stagnation and reattachment and a nearly uniform temperature were detected in the core region. The self-merger is the result of the pressure deficit existing between the external ambient fluid and the annular core. This deficit draws the annular plumes to the centreline (Coandă effect). Beyond the core region, the mean axial velocities and mean temperatures for each set were measured and predicted at several axial distances along the plume centreline.

An original integral model for the prediction of the self-merging trajectory of the annular plume, briefly named SMA, is developed. SMA has two main points of interest that deserve to be highlighted: (a) The validity that two anti-diametrical plane plumes are equivalent to the annular plume in the core region is justified by the method of conformal mapping, which also helps to determine the applicability limits of SMA. SMA predictions are acceptable for diameter ratio of annular plume $d_0/D_0 \leq O(0.1)$, which is approximately equivalent to the range $1 < D_{out}/D_{in} < 2$. (b) Calculation of sink strength and volume flux in the self-merging region requires the external analytical functions (10) and (11) proposed herein. In general, SMA predictions are compared with the experimental data and the accuracy is satisfactory.

For $w_0 = 0.527$ m/s, the reattachment location P_0 is experimentally detected at $z_{P0} = 16.1d_0$, while SMA predicts it at $z_{P0} = 16.0d_0$. For $w_0 = 0.702$ m/s, P_0 is experimentally detected at $z_{P0} \cong 20d_0$, while SMA predicts it at $z_{P0} = 20.7d_0$. Both predictions are very close to the experimental values. The present experiments indicated that the location of the maximum upward velocity at the centreline of annular plumes does not coincide with the reattachment location, in contrast to the annular jets with high initial velocities. This fact is attributed to the waving and flickering of the self-merging trajectories of the annular core due to low momentum and disturbances induced by the vortex ring. Another finding is that the outer entrainment and the entrainment starvation from the internal boundaries of the equivalent 2D plumes contribute to the convergence limit by 99% and only 1% is owed to the flow potential.

With the aid of dimensional analysis, the reattachment point, z_{P0}, is successfully correlated with the dimensionless independent variables of the initial Froude number F_0 and the annulus diameter ratio D_{out}/D_{in}. It is found that the normalised dimensionless reattachment distance $Z_{P0} = (z_{P0}/d_{eq})F_0^{-1}$ is practically constant, $Z_{P0} = 1.38 \pm 0.05$ in the region $1 < D_{out}/D_{in} \leq 2$, meaning that z_{P0} is mainly proportional to F_0 and d_{eq}.

Experimental observations reveal that a vortex ring is generated within the core region, occupying the area up to the level $z \cong 5.5d_0$ for both sets examined. The vorticity of the annular plume propagates a downward velocity at the plume centreline. The velocity direction was detected using a very thin nylon strip, which was initially directing downwards for $0 \leq z < 5.5d_0$ and changed abruptly to the upward direction for $z \geq 5.5d_0$ (see description on **movie1** in "Appendix 1"). The centreline velocity was measured, and its minimum (downward maximum) value − 0.926 m/s occurred at the level $z = 2.742d_0$ for the set with $w_0 = 0.527$ m/s and − 1.027 m/s at $z = 3.5d_0$ for $w_0 = 0.702$ m/s. This centreline location should get the lowest atmospheric pressure. The location $z \cong 5.5d_0$, where the centreline velocity changes direction, defines the stagnation point. The experimental measurements of the mean axial velocity at the

plume centreline show that the stagnation point is located at $z_{P1} = 5.42d_0$ for the set with $w_0 = 0.527$ m/s and at $z_{P1} = 5.51d_0$ for $w_0 = 0.702$ m/s. The good stability of the stagnation point is a matter of related stability of the vortex ring due to the solid bottom, which prevents the downward motion of the vortex ring.

The axisymmetric mode of SMA is used to predict the centreline mean axial velocities and mean concentrations of the annular plume. The predictions are compared with the experimental measurements and are in very good agreement for $Z \geq 5$, regarding velocities and concentrations, while they overestimate the velocities and concentrations for $Z < 5$ and $Z < 4$, correspondingly. In addition, the above centreline quantities are predicted using the superposition method (SM) and the results are also compared with the experimental measurements and SM predictions and are in excellent agreement with the experimental data for $Z \geq 2$.

The research ends up with some implications regarding the sensitivity of critical parameters used in the models. The use of suitable equations in SMA is mainly understood by the smoothness of convergence towards the measured intersection point in predicting the self-merging of the annular plume and, additionally, by the physical realism of the model and its ability to accurately predict laboratory measurements. Another critical point is the use of air densities based on the standard atmosphere. The sensitivity analysis shows that the use of dry air densities instead of densities of wet air with an average relative humidity 55% may result to errors − 21.2% in SMA predictions of the reattachment point P_0. The errors made in the centreline velocity predictions at $z = 60d_0$ are 9.6% and 11.4%, and for the concentrations − 10.2% and − 12.9%, regarding SMA and SM, correspondingly. The relative error of SMA prediction for dry air conditions against the measured value for the reattachment point P_0 is 0.6%. The corresponding errors for the centreline mean velocities and mean concentrations at $z = 60d_0$ are − 14.7% and − 8.6% for SMA, while 4.6% and 4.8% for SM predictions.

For practical purposes, it is implied that the annular plume constitutes the limiting case of the equivalent rosette-type diffuser, which may be used in the design of systems for wastewater disposal in the ocean. In the case of discharges in deep water bodies, the annulus-type diffuser, which is equivalent to a rosette-type diffuser, succeeds at the water surface approximately equal dilutions to the rosette-type diffuser and the equivalent round plume for equal flow rates. In shallow water bodies, the annulus-type diffuser may achieve about 15 times (on average) higher centreline dilutions than the corresponding bulk dilutions of the round plume. This result is due to the better mixing in the core region owed to the vortex ring, the increase of the outer entrainment due to the pressure drop inside the core and the longer diameter of the ring exit.

The present research may help engineers, model developers and project designers dealing with wastewater disposal systems into water bodies or air-pollutant and cooling-tower emissions into the atmosphere, to scientifically support decision-making and management practices.

Appendix 1: Description of the video movie1.mp4

The velocity transducer is unable to detect the velocity direction. Therefore, a visual method was used to detect the centreline location where axial velocities change direction. For the basic case of initial velocity $w_0 = 0.527$ m/s, the procedure was recorded

in the video named **movie1.mp4** and it can be observed frame-by-frame. Initially, a black cardboard was installed behind the flow field, about 20 cm away from the plume centreline and a narrow strip of white cardboard marked every 1 cm was placed 2 cm behind the plume centreline, both in the vertical direction. Care was paid to fixing the marked strip so that the zero level was accurately at the level of the ring exit. Then, a video camera was fixed on a tripod about 50 cm in front of the plume centreline and at the same level as the location of the phenomenon to be recorded. Putting the device in normal operation, a very thin nylon strip tethered in a stretched thread was moving at the plume centreline vertically from up to down. It is observed that the thin nylon strip was directing upwards over the level of 5.5 cm and at this level changed abruptly the direction, which was maintained all the way downward. This video is accompanying the paper.

Appendix 2: Measurement details—Tables

Prior to the experimental measurements, the hot air production system was activating. The measurements always started twenty minutes after turning the setup on, to allow the temperature stabilization in the air heating box. At the cross-sections of the nozzle exit, the temperatures were recorded for 84 min, using the HH147 OMEGA thermometer with four thermistors. The air temperature variation was determined at each cycle of the electronic controller. The thermistors were placed at the four cross-sectional locations $x = -x = y = -y = 6$ cm of the nozzle exit. Each thermistor recorded the mean value of temperature per 1 min time interval. The result is that the average value and standard deviation of the mean air temperature level at the exit were kept at 68.5 ± 3.81 °C and the cycle duration was about 3 min and 55 s on the warm summer days or approaching 3 min during cold days of the year. It is important to notice that the room was thermally well insulated, while the renewal of the room air was extremely slow during the experiments because all openings were kept closed. The room and chamber temperature at the beginning of the measurements was uniform. The increase of the background mean temperature of the room air from the beginning to the end of each-day measurements (duration of 7.5 h, approximately) was less than 2.0 °C, which causes a gradual reduction of the effective gravitational acceleration g'_0 up to 5%, approximately. Similarly, continuous temperature measurements of the background air environment inside the experimental chamber were recorded at the levels 0.25 m, 0.75 m, 1.25 m, and 1.75 m above the floor, in order to check the degree of the air uniformity during the experimental measurements. The air temperature at the level of 1.75 m of the chamber background, compared to the temperature at 0.25 m, was found less than 1 °C higher. The average relative humidity inside the room during the measurement hours was 55%. A 1 °C-temperature increase causes a weak stratification of air density (density slope -2.67×10^{-3} kg/m^4). According to the annular plume characteristics and applying the experimental results by Ogino et al. [59], it is estimated that the plume would be trapped by the density interface and to outflowed horizontally at the level 4.36 m above the floor, which is higher than the ceiling level being at 2.89 m. Consequently, it was not expected nor observed any plume entrapment during the measurements conducted. It is noted that the maximum level for the measurements was 2.34 m above the floor. If the system of the room and the buoyant source is considered as a filling box, it is useful to determine the characteristic time needed for the air volume of the room to pass through the system of the air compressor-heating box. According to Baines and Turner

Table 6 Statistical data of centreline axial velocity measurements in the core region of the annular plume with $w_0 = 0.527$ m/s

Run	z (cm)	w_m (mm/s)	w_{min} (mm/s)	w_{max} (mm/s)	$\pm s$ (mm/s)	n	T_a (°C)	F_0
V1.1	10.0	754	689	811	36	23	23.0	1.63
	15.0	650	601	689	28	19		
V1.2	11.0	703	637	742	31	22	19.5	1.56
	16.0	624	585	657	25	22		
V1.3	7.0	835	712	932	59	36	18.0	1.53
	8.0	785	697	875	43	36		
	9.0	754	667	831	41	36		
	10.0	748	637	818	44	36		
	12.0	702	589	760	47	36		
	14.0	686	587	756	42	36		
	16.0	663	589	735	40	36		
	18.0	640	539	738	48	36		
V1.4	7.0	801	663	916	66	36	23.0	1.63
	8.0	753	639	874	56	36		
	10.0	694	597	783	58	36		
	12.0	681	590	740	50	36		
	14.0	651	547	697	42	36		
	16.0	613	539	668	40	36		
V1.5	1.0	− 299	− 350	− 263	17	36	26.0	1.70
	1.5	− 366	− 409	− 336	19	39		
	2.0	− 361	− 389	− 336	17	36		
	3.0	− 437	− 481	− 389	24	36		
	4.0	− 388	− 426	− 354	23	44		
	5.0	− 258	− 281	− 234	13	36		
	6.0	265	217	318	24	36		
	6.5	498	409	600	44	36		
	7.0	769	673	830	44	36		
V1.6	7.5	871	755	959	53	40	26.0	1.70
	8.0	750	680	806	38	36		
	10.0	705	646	759	36	36		
	12.0	673	612	720	28	36		
	14.0	654	572	704	35	45		
	16.0	646	593	688	30	36		

[60] and Caulfield and Woods [61], based on the data given above, this time is longer than 15 h for both flow rates used. As the experiments took place in the cylindrical chamber, the plume, a little lower than the ceiling and over the chamber, spread horizontally and mixed with the air of the room mainly outside the chamber. The chamber was supplied with the cold air of the room from the radial entrance gap near the floor (Fig. 2). The air temperature in the gap remained slightly less (≤ 0.5 °C) than the mean temperature of the background air of the chamber due to the slight stratification of the room air. The time needed for steady-state temperature in the room air is estimated to be more than 11 h [62]. Thus, the plume characteristics remained practically unaffected by the filling box effect.

Table 7 Statistical data of centreline axial velocity measurements in the core region of the annular plume with $w_0 = 0.702$ m/s

Run	z (cm)	w_m (mm/s)	w_{min} (mm/s)	w_{max} (mm/s)	$\pm s$ (mm/s)	n	T_a (°C)	F_0
V1.7	0.5	− 251	− 273	− 234	16	19	21.2	2.12
	1.0	− 386	− 424	− 364	20	19		
	2.0	− 515	− 542	− 482	18	19		
	3.0	− 676	− 711	− 631	25	19		
	4.0	− 675	− 726	− 633	25	19		
	5.0	− 378	− 405	− 333	20	19		
	6.0	483	552	405	44	20		
	7.0	865	786	943	48	19		
	8.0	1035	916	1115	66	18		
	9.0	1029	910	1115	62	19		
	10.0	985	842	1065	74	20		
	12.0	886	772	966	62	19		
	14.0	827	751	883	39	19		
	16.0	799	701	873	54	19		
	18.0	762	672	842	50	19		
	20.0	758	672	842	59	19		
	22.0	740	652	811	50	19		

The velocity was measured at several levels along the vertical z-axis in the annular plume centreline. Velocity measurements were also made in both x and y directions of several cross-sections of the main flow. For performing the latter measurements, the air velocity transducer was mounted within a cardboard hollow cylinder, as proposed by Stefanidou et al. [42]. The main experiments were carried out with the flow rate $\mu_0 = 1986$ cm^3/s, which provided mean velocity $w_0 = 52.7$ cm/s at the exit. In addition, another set of axial velocity measurements was carried out with flow rate $\mu_0 = 2646$ cm^3/s providing a mean exit velocity $w_0 = 70.2$ cm/s. To get a reliable mean axial velocity value for each measurement in a prescribed point of the flow field, the recording duration was set at least to 6 min, providing 36 values of 10-s time step with 10-s averaging time for each value. Reliability checks of the velocity transducer performed at the plume centreline showed that the error was less than 10%. Tables 6 and 7 include the statistical data of the experimental axial velocity measurements at the plume centreline in the core region for $w_0 = 0.527$ m/s and 0.702 m/s, correspondingly, along with the measurement conditions. Tables 8 and 9 include the corresponding measurements beyond the core region. Table 10 includes the data for the trajectory of merging. For the verification of the measurement reliability of velocities, several runs of measurements were repeated.

The temperatures were measured at several levels z. At each level, simultaneous temperature measurement was made at the whole cross-section. The computer recorded one instant temperature value per second at each thermistor location, simultaneously for all thermistors. The temperature measurement procedure was very simple. Initially, the system of thermistors was located and fixed at the required level for measurements. Before turning the system of the hot air production on, the system of thermistors is turned on and was recording the room air temperature for about 20

Table 8 Statistical data of the centreline axial velocity measurements beyond the core region of the annular plume with $w_0 = 0.527$ m/s

Run	z (cm)	w_m (mm/s)	w_{min} (mm/s)	w_{max} (mm/s)	$\pm s$ (mm/s)	n	T_a (°C)	F_0
V1.1c	20	605	565	643	25	24	23.0	1.63
	25	593	549	622	23	20		
	30	593	557	625	20	21		
	35	601	565	649	22	22		
	40	610	536	639	22	22		
	45	620	586	648	17	25		
	50	624	596	664	19	23		
	60	614	591	645	16	25		
	70	591	581	612	7	21		
	80	569	548	588	12	23		
	90	548	534	565	10	23		
	100	518	496	539	12	27		
	110	498	476	523	13	23		
	120	502	476	523	14	24		
	130	487	466	510	12	23		
	140	482	453	513	15	22		
V1.2c	21	605	543	653	30	22	19.5	1.56
	26	601	540	642	25	21		
	36	639	572	709	35	22		
	46	650	617	678	17	23		
	56	630	601	656	15	22		
	76	554	538	575	10	23		
V1.3c	18	640	539	738	48	36	18.0	1.53
	20	630	549	685	36	36		
	22	608	539	676	35	36		
	24	600	525	696	41	36		
	26	595	530	652	37	36		
	29	599	510	652	35	36		
	32	600	538	664	31	36		
	35	610	553	752	40	36		
	40	616	546	711	44	36		
	45	635	583	746	34	36		
	50	633	589	691	27	40		
	55	633	580	686	26	36		
	60	626	582	668	22	36		
	65	627	593	661	16	36		
	70	610	578	643	16	36		
	75	610	568	634	17	36		
	80	589	563	624	17	36		
	85	578	536	627	21	36		
V1.4c	19	587	506	653	45	36	23.0	1.63
	22	571	495	623	38	36		

Table 8 (continued)

Run	z (cm)	w_m (mm/s)	w_{min} (mm/s)	w_{max} (mm/s)	$\pm s$ (mm/s)	n	T_a (°C)	F_0
	25	567	494	632	36	36		
	30	580	506	642	29	36		
	35	596	525	685	34	36		
	40	607	545	664	33	36		
	45	629	583	681	22	36		
	50	625	584	661	20	36		
	55	632	583	656	17	36		
	60	628	583	653	15	36		
	65	622	591	675	17	36		
	70	604	554	638	18	36		
	75	592	561	611	12	36		
	80	577	545	619	15	36		
	85	575	554	604	14	36		
	90	546	508	604	20	36		
	95	531	486	558	19	36		
	100	526	483	554	18	36		
	105	511	480	561	19	36		
	110	510	476	550	19	36		
	115	507	458	539	18	36		
	120	503	454	546	21	36		
	125	497	456	535	18	36		
	130	481	413	532	25	36		
V1.6c	20	575	512	628	30	36	26.0	1.70
	30	591	528	662	36	48		
	40	619	562	662	29	36		
	50	604	554	652	22	36		
	60	567	544	612	17	40		
	70	541	476	588	24	36		
	80	495	388	552	34	36		
	90	543	512	565	16	36		
	100	513	473	546	20	36		
	110	491	404	530	22	36		
	120	490	422	528	25	36		
	130	475	407	518	24	39		
	140	467	430	512	19	36		
	150	446	371	496	31	36		
	160	446	371	480	23	36		
	170	437	388	464	20	36		
	180	423	371	470	25	36		
	190	419	347	457	27	36		
	200	434	371	476	22	36		
	210	410	371	455	21	38		

Table 9 Statistical data of the centreline axial velocity measurements beyond the core region of the annular plume, with $w_0 = 0.702$ m/s

Run	z (cm)	w_m (mm/s)	w_{min} (mm/s)	w_{max} (mm/s)	$\pm s$ (mm/s)	n	T_a (°C)	F_0
V1.7c	20	752	398	508	27	36	19.5	2.08
	25	738	388	510	31	36		
	30	733	388	483	26	36		
	40	735	397	497	27	36		
	50	734	409	497	19	36		
	60	710	409	445	10	36		
	70	654	367	409	11	36		
	80	638	357	409	12	36		
	90	630	357	399	9	36		
	100	591	327	383	13	36		
	110	576	320	367	12	36		
	120	553	306	357	12	36		
	130	539	296	347	14	36		
	140	529	262	351	22	46		
	150	508	268	327	14	36		
	160	497	260	330	16	36		
	170	479	259	317	17	36		
	180	483	239	317	20	36		
	190	463	250	306	14	36		
	200	462	229	308	18	36		
	210	453	240	306	13	62		

min. This measurement was used to set a common calibration level for all thermistors. The time interval for reliable temperature measurements was at least 35 min for a cross-section. For each thermistor location, the number of values, the average, the min/max values, and the standard deviation have been calculated. Table 11 includes the statistical data regarding the temperature measurements in the core region along the plume centreline, accompanied by the measurement conditions, and Table 12 the maximum temperatures and their location, for $w_0 = 0.527$ m/s. Table 13 includes the temperatures along the plume centreline beyond the core region for $w_0 = 0.527$ m/s. It is noted that the temperature measurements were repeated some months later for reliability verification.

Appendix 3: Mathematical justification of the self-merging of the annular plume to resemble that of two-plane plumes

The assumption made in Sect. 3.2, saying that the two infinitesimal sectors of the core region of the annular plume may be considered as two plane plumes, is supported by the method of conformal mapping [63, 64]. In the complex plane, which is defined by the real axis x and the imaginary axis y, it is plotted a strip

Table 10 Statistical data of the trajectory location in the core region of the annular plume with $w_0 = 0.527$ m/s

Run	z (cm)	r_m (cm)	r_{min} (cm)	r_{max} (cm)	T_a (°C)	F_0
VT0	0.00	5.77	5.77	5.77	19.0	1.55
VT2	2.00	5.50	5.50	5.50	25.2	1.68
VT3	3.75	4.38	4.00	5.00	19.6	1.56
VT4	4.00	4.63	3.50	5.00	24.2	1.66
VT5	5.00	4.38	3.50	5.50	21.8	1.61
VT6	6.00	3.88	3.50	4.00	23.2	1.64
VT7	7.50	1.25	1.00	2.00	21.8	1.61
VT8	8.00	2.88	2.50	3.50	25.1	1.67
VT9	9.00	1.50	0.00	3.00	23.6	1.64
VT10	10.00	2.25	1.00	3.50	24.8	1.67
VT11	11.00	2.00	0.00	3.00	23.5	1.64
VT12	12.00	1.50	0.00	3.50	24.7	1.67
VT13	13.00	1.50	0.00	3.00	23.4	1.64
VT14	14.00	1.00	0.00	2.00	23.9	1.65
VT15	15.00	0.75	0.00	1.00	19.8	1.57

Table 11 Statistical data of the centreline temperature measurements in the core region of the annular plume with $w_0 = 0.527$ m/s

Run	z (cm)	T_m (°C)	T_{min} (°C)	T_{max} (°C)	$\pm s$ (°C)	n	T_a (°C)	F_0
T1.1	2.00	60.88	56.67	65.30	2.04	8936	32.5	1.86
T1.2	5.00	63.01	58.29	68.09	2.42	3650	32.9	1.87
T1.3	7.50	63.24	58.39	68.09	2.56	3668	33.0	1.88
T1.4	10.00	62.28	56.70	67.30	2.44	7074	32.6	1.87
T1.5	15.00	61.67	57.19	66.09	2.46	2087	32.8	1.87
T1.6	16.00	61.04	56.40	66.10	2.37	3537	32.3	1.86
T4.1	3.75	58.91	53.38	65.45	2.76	5338	20.0	1.57
T4.2	5.00	58.53	51.68	65.15	3.01	5346	20.1	1.57
T4.3	15.00	57.17	52.15	61.75	2.32	2669	20.1	1.57

$S = z = x + iy \mid b \le x \le a, -\pi \le y \le \pi$, where $a = \log(R_1)$ and $b = \log(R_2)$; R_1, R_2 are the lengths of the outer and inner radius of the cross-section of the core region of the annular plume at level $z > 0$. It is assumed that a horizontal entrainment velocity u_{B0} is applied in the outer boundary on the right of strip S, as shown in Fig. 19a. The complex function $\zeta = e^z$ maps the strip S to the annulus $A = \zeta = \eta + i\psi \mid R_1, R_2$, and the field of horizontal entrainment velocities u_{B0} to the radial velocities u_{B1} applied in the outer boundary of the annular plume, as shown in Fig. 19b. It is noted that this is a one-to-one mapping. The same function maps the source strip $S_0 = z = x + iy \mid b_0 \le x \le a_0, -\pi \le y \le \pi$ to the annular source $A_0 = \zeta = \eta + i\psi \mid D_{out}/2, D_{in}/2$, where $a_0 = \log(D_{out}/2)$ and $b_0 = \log(D_{in}/2)$; D_{out}, D_{in} are the lengths of the outer and inner diameter of the cross-section of the annular source. The field point $P(x, y)$ is mapped to $P(\eta, \psi)$ in Cartesian or $P(r, \theta)$ in polar coordinates. The outer boundaries of cross-sections are shown in Fig. 19 with brown dashed line and large dots, which are numbered from 1 to 8, while the inner boundaries with blue dashed line and the mean diameter of the plume source is plotted by a dot-dash-dot red line. The red point $A(\frac{a_0-b_0}{2}, 0)$ of the strip at the source centreline is mapped to the red point $A(\frac{D_{out}-D_{in}}{2}, 0)$ at the centre of the annular slot. The black points at the source centreline of the strip, $B_1(\frac{a_0-b_0}{2}, \frac{L_s}{2})$ and $B_2(\frac{a_0-b_0}{2}, -\frac{L_s}{2})$, are mapped to the same black point $B_1(\frac{D_{out}-D_{in}}{2}, \pi) \equiv B_2(\frac{D_{out}-D_{in}}{2}, -\pi)$ at the centre of the annular slot. The large brown dots numbered from 1 to 8 at the strip boundary on the right are mapped to the large brown dots at the outer boundary of the annular plume following one-to-one the corresponding numbering.

The boundary conditions (like entrainment) are 2π-periodic functions of the angle θ of the polar coordinate system $O(r, \theta)$ shown in Fig. 19b. Thus, the solution made in the 2D problem with entrainment extended along the boundary on the right of the strip is mapped on the outer boundary of the annulus. Experimental evidence has shown that the 2D behaviour of a slot diffuser of a finite length is maintained up to a level approximately equal to the diffuser length [46, 65]. Since the 2D behaviour of each plane plume of slot width d_0 should be extended at least up to the reattachment location z_{P0}, the length L_s of a finite slot should be at least $L_s \approx z_{P0}$ or $L_s/z_{P0} = O(1)$. Thus, as $z_{P0}/d_0 = O(10)$, it is implied that $L_s/d_0 = O(10)$; for the strip shown in Fig. 19a representing the slot source of the plane plume with width $(a_0 - b_0)$ and length $L_s = 2\pi$, the strip aspect ratio

Table 12 Statistical data of the measurements of maximum temperatures and their location at several cross-sections of the core region of the annular plume with $w_0 = 0.527$ m/s

Run	z (cm)	r_m (cm)	T_m (°C)	T_{min} (°C)	T_{max} (°C)	$\pm s$ (°C)	n	T_a (°C)	F_0
TT0	0.00	6.0	68.50	63.43	74.09	3.00	264	32.5	1.86
TT2	2.00	5.8	68.27	62.57	75.07	3.19	8936	32.5	1.86
TT5.1	5.00	2.0	63.58	59.03	67.43	1.97	3539	32.1	1.85
	5.00	2.0	60.68	56.17	64.87	1.86	3539	32.1	1.85
TT5.2	5.00	3.0	63.33	58.79	67.49	2.31	1825	32.9	1.87
TT7	7.50	0.0	63.24	58.39	68.09	2.56	3668	33.0	1.88
TT10	10.00	0.0	62.28	56.70	67.30	2.44	7074	32.6	1.87
TT15	15.00	0.0	61.67	57.19	66.09	2.46	2087	32.8	1.87
TT16	16.00	0.0	61.04	56.40	66.10	2.37	3537	32.3	1.86
TT3	3.75	2.9	58.91	53.47	64.12	2.57	5338	20.0	1.57
TT5.3	5.00	2.9	57.74	50.27	65.22	3.61	5346	20.1	1.57
TT15.2	15.00	0.0	57.17	52.15	61.75	2.32	2669	20.1	1.57

Table 13 Statistical data of the centreline temperature measurements beyond the core region of the annular plume with $w_0 = 0.527$ m/s

Run	z (cm)	T_m (°C)	T_{min} (°C)	T_{max} (°C)	$\pm s$ (°C)	n	T_a (°C)	F_0
T1.7	25	57.28	50.63	61.83	2.29	3537	32.40	1.86
T1.8	30	54.40	48.29	59.69	2.49	1804	33.00	1.88
T1.9	40	50.25	44.19	55.49	1.99	3066	32.45	1.86
T1.10	60	44.66	40.19	48.19	1.49	1804	33.00	1.88
T1.11	80	41.21	38.19	44.19	1.13	1953	32.90	1.87
T1.12	90	39.72	36.19	42.39	0.96	1872	32.85	1.87
T1.13	100	39.28	35.79	41.99	0.89	7122	32.85	1.87
T1.14	120	37.36	34.89	39.49	0.74	1872	32.50	1.86
T1.15	140	36.94	33.93	38.73	0.57	3396	32.70	1.87
T1.16	160	36.55	34.83	37.93	0.42	3664	32.90	1.87
T1.17	180	36.12	33.67	37.67	0.66	3415	34.10	1.91
T1.18	190	36.34	35.03	37.43	0.37	3415	34.10	1.91
T4.4	20	54.71	49.45	58.85	2.22	2670	19.93	1.57
T4.5	40	43.13	36.85	48.75	1.85	2668	19.73	1.57
T4.6	50	38.66	32.72	43.02	1.50	2667	19.73	1.57
T4.7	60	34.67	28.45	39.25	1.48	5316	19.70	1.57
T4.8	70	32.03	26.05	35.75	1.20	8055	19.53	1.56
T4.9	80	30.25	26.55	33.72	0.96	8007	19.35	1.56
T4.10	90	28.33	22.76	31.62	1.06	8004	19.33	1.56
T4.11	100	27.35	23.65	29.85	0.84	8013	19.30	1.56
T4.12	110	26.17	22.32	28.92	0.84	8013	19.23	1.56
T4.13	120	25.14	22.34	27.19	0.70	2672	18.98	1.55
T4.14	130	23.92	19.92	26.12	0.74	2686	18.50	1.54
T4.15	140	24.36	21.78	26.58	0.59	8010	19.73	1.57
T4.16	150	23.69	21.25	25.88	0.60	8007	19.55	1.56
T4.17	160	23.16	21.68	24.88	0.48	8010	19.35	1.56
T4.18	170	22.80	21.25	24.48	0.45	7995	19.38	1.56
T4.19	180	22.28	20.65	23.98	0.47	7920	19.25	1.56
T4.20	190	21.73	20.28	23.28	0.41	7911	19.03	1.55
T4.21	201	21.12	18.98	22.68	0.47	8016	18.83	1.55

is $L_s/(a_0 - b_0) = 2\pi/\log(D_{out}/D_{in}) = O(10)$. Solving the latter equation with respect to D_{out}/D_{in}, one gets $D_{out}/D_{in} \approx 1.9$ or, equivalently, $d_0/D_0 \leq 0.31$; d_0, D_0 are the slot width and the mean diameter of the annular source, correspondingly. This means that a solution for well predicting z_{P0} using plane plumes is efficient for annular plume sources with diameter ratios in the range $1 < D_{out}/D_{in} < 2$. Based on the above justification, it is concluded that the assumption made in Sect. 3.2 is valid for the cases studied herein.

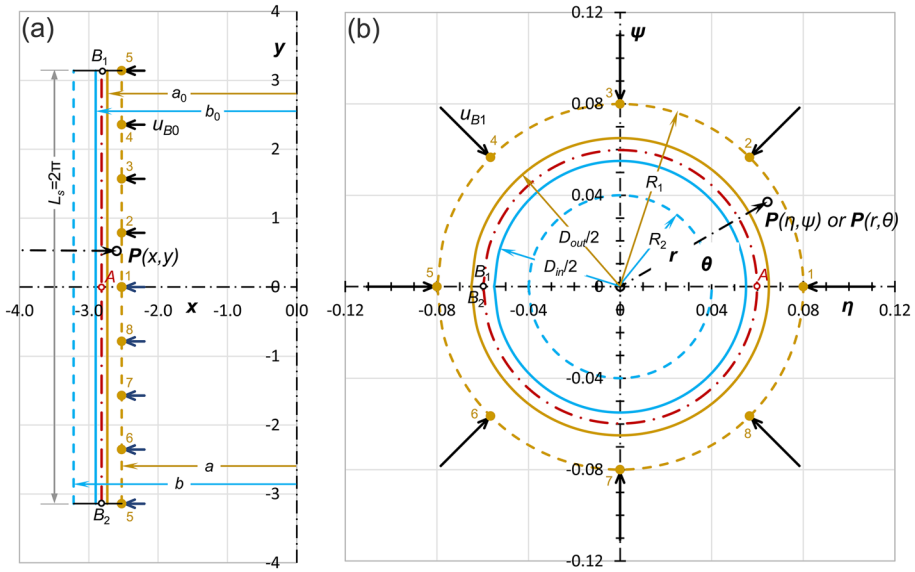

Fig. 19 Conformal mapping of strip **a** along with the field of the entrainment velocities u_{B0} to annulus **b** along with the corresponding field of the radial entrainment velocities u_{B1}

Supplementary Information The online version contains supplementary material available at https://doi.org/10.1007/s10652-023-09943-z.

Acknowledgements The authors thank EEL for the disposal of equipment and the support of the research performed in the context of the completion of the Ph.D. of Maria K. Stefanidou. They also thank the Research Engineer at Stevens Institute of Technology Dr. Christos P. Giannopoulos for additional paper enhancements, as well as the University Network HYDROCRITES and the National Observatory of Athens for the provision of necessary meteorological data. Finally, the authors acknowledge the review provided by the EFMC Associate Editor Prof. Scott A. Socolofsky and the three reviewers; thanks to their scrutinised comments contributed to substantial improvements of the paper.

Funding Open access funding provided by HEAL-Link Greece.

Declarations

Conflict of interest The authors report no conflict of interest.

References

1. Yang C, Li A, Gao X, Ren T (2020) Interaction of the thermal plumes generated from two heat sources of equal strength in a naturally ventilated space. J Wind Eng Ind Aerodyn 198:104085. https://doi.org/10.1016/j.jweia.2019.104085
2. Turner JS (1973) Buoyancy effects in fluids. Cambridge University Press, Cambridge. ISBN 9780511608827
3. Wilson L, Sparks RSJ, Huang TC, Watkins ND (1978) The control of volcanic column heights by eruption energetics and dynamics. J Geophys Res 83(B4):1829–1836. https://doi.org/10.1029/JB083iB04p01829
4. Turner JS (1986) Turbulent entrainment: the development of the entrainment assumption, and its application to geophysical flows. J Fluid Mech 173:431–471. https://doi.org/10.1017/S0022112086001222
5. Chen Z, Li Y, Liu Z, Wang J, Zhou X, Du J (2018) Radon emission from soil gases in the active fault zones in the Capital of China and its environmental effects. Sci Rep 8:16772. https://doi.org/10.1038/s41598-018-35262-1
6. Slawson PR, Csanady GT (1967) On the mean path of buoyant, bent-over chimney plumes. J Fluid Mech 28:311–322. https://doi.org/10.1017/S0022112067002095
7. Li S, Flynn MR (2021) Cooling tower plume abatement and plume modeling: a review. Environ Fluid Mech 21:521–559. https://doi.org/10.1007/s10652-021-09790-w
8. Fischer HB, List EJ, Koh RCY, Imberger J, Brooks NH (1979) Mixing in inland and coastal waters. Academic Press, San Diego
9. Jirka GH (2008) Improved discharge configurations for brine effluents from desalination plants. J Hydraul Eng 134(1):116. https://doi.org/10.1061/(ASCE)0733-9429(2008)134:1(116)
10. Roberts PJ, Tian X, Jung Y (2011) Physical model study of an alternating diffuser for thermal discharge. J Hydraul Eng 137(9):1027–1036. https://doi.org/10.1061/(ASCE)HY.1943-7900.0000378
11. Roberts PJW, Salas HJ, Reiff FM, Libhaber M, Labbe A, Thomson JC (2010) Marine wastewater outfalls and treatment systems. IWA, London
12. Chow WK, Li J (2007) Numerical simulations on thermal plumes with $k-\varepsilon$ types of turbulence models. Build Environ 42(8):2819–2828. https://doi.org/10.1016/j.buildenv.2005.12.006
13. Nam S, Bill RG (1993) Numerical simulation of thermal plumes. Fire Saf J 21(3):231–256. https://doi.org/10.1016/0379-7112(93)90029-P
14. Durrani F, Cook MJ, McGuirk JJ (2012) Modelling buoyant thermal plumes in naturally ventilated buildings. In: Proceedings of the first building simulation and optimization conference, 10–11 September 2012. Loughborough University, pp 117–123
15. Linden PF, Lane-Serff GF, Smeed DA (1990) Emptying filling boxes: the fluid mechanics of natural ventilation. J Fluid Mech 212:309–335. https://doi.org/10.1017/S0022112090001987
16. Fontaine JR, Devienne R, Rose S (2006) Numerical simulation and experimental validation of plume flow from a heated disk. Numer Heat Transf Part A Appl 50(7):645–666. https://doi.org/10.1080/10407780600650720
17. Bjørn E, Nielsen PV (1995) Merging thermal plumes in the indoor environment. Dept. of Building Technology and Structural Engineering, Indoor Environmental Technology, R9541, vol 54
18. Ko NWM, Chan WT (1978) Similarity in the initial region of annular jets: three configurations. J Fluid Mech 84(4):641–656. https://doi.org/10.1017/S0022112078000397
19. Chan WT, Ko NWM (1978) Coherent structures in the outer mixing region of annular jets. J Fluid Mech 89(3):515–533. https://doi.org/10.1017/S0022112078002712
20. Ko NWM, Chan WT (1979) The inner regions of annular jets. J Fluid Mech 93(3):549–584. https://doi.org/10.1017/S0022112079002652
21. Aly MS, Rashed MII (1991) Experimental investigation of an annular jet. J Wind Eng Ind Aerodyn 37:155–166. https://doi.org/10.1016/0167-6105(91)90070-D
22. Warda HA, Kassab SZ, Elshorbagy KA, Elsaadawy EA (1999) An experimental investigation of the near-field region of free turbulent round central and annular jets. Flow Meas Instrum 10:1–14. https://doi.org/10.1016/S0955-5986(98)00042-9
23. Patte-Rouland B, Lalizel G, Moreau J, Rouland E (2001) Flow analysis of an annular jet by particle image velocimetry and proper orthogonal decomposition. Meas Sci Technol 12:1404–1412. https://doi.org/10.1088/0957-0233/12/9/305
24. Danlos A, Lalizel G, Patte-Rouland B (2013) Experimental characterization of the initial zone of an annular jet with a very large diameter ratio. Exp Fluids 54:1–17. https://doi.org/10.1007/s00348-012-1418-x

25. Patte-Rouland B, Danlos A, Rouland E (2013) Annular jet instabilities and stagnation point. Control of instabilities by modification of the central obstacle. In: Advances in modern mechanical engineering, pp 140–145. ISBN: 978-960-474-307-0
26. Padhani SA, Hunt GR, Jukes TN (2018) Turbulent jet from a slender annular slot ventilated by a self-induced flow through the open core. Phys Rev Fluids 3:1–32. https://doi.org/10.1103/PhysRevFluids.3.014602
27. Wang Y, Huang Y, Liu J, Wang H, Liu Q (2013) Flow-field characteristics of high-temperature annular buoyant jets and their development laws influenced by ventilation system. Sci World J 2013, Article ID 826514, 11 p. https://doi.org/10.1155/2013/826514
28. Seo W II, Yeo HK (2002) Near-field dilution of rosette type multiport wastewater diffusers. Water Eng Res 3(2):93–111
29. Seo Ii W, Kwon SJ, Yeo HK (2004) Merging characteristics of buoyant discharges from Rosette-type diffusers in shallow water. KSCE J Civ Eng 8(6):679–688. https://doi.org/10.1007/BF02823559
30. Kwon SJ II, Seo W (2005) Experimental investigation of wastewater discharges from a rosette-type riser using PIV. KSCE J Civ Eng 9(5):355–362. https://doi.org/10.1007/BF02830626
31. Lai ACH, Yu D, Lee JHW (2011) Mixing of a rosette jet group in a crossflow. J Hydraul Eng 137(8):787–803. https://doi.org/10.1061/(ASCE)HY.1943-7900.0000359
32. Abessi O, Roberts PJW, Gandhi V (2016) Rosette diffusers for dense effluents. J Hydraul Eng. https://doi.org/10.1061/(ASCE)HY.1943-7900.0001268
33. Yan X, Mohammadian A, Chen X (2019) Three-dimensional numerical simulations of buoyant jets discharged from a rosette-type multiport diffuser. J Mar Sci Eng 7:409, 15 p. https://doi.org/10.3390/jmse7110409
34. Favre-Marinet M, Schettini EBC (2001) The density field of coaxial jets with large velocity ratio and large density differences. Int J Heat Mass Transf 44:1913–1924. https://doi.org/10.1016/S0017-9310(00)00240-4
35. Li S, Moradi A, Vickers B, Flynn MR (2018) Cooling tower plume abatement using a coaxial plume structure. Int J Heat Mass Transf 120:178–193. https://doi.org/10.1016/j.ijheatmasstransfer.2017.12.040
36. Li S, Flynn MR (2020) Coaxial plumes in a windy ambient with applications to cooling towers. J Wind Eng Ind Aerodyn 196, 17 p. https://doi.org/10.1016/j.jweia.2019.104054
37. Papanicolaou PN, List EJ (1987) Statistical and spectral properties of tracer concentration in round buoyant jets. Int J Heat Mass Transf 30(10):2059–2071. https://doi.org/10.1016/0017-9310(87)90086-X
38. Papanicolaou PN, List EJ (1988) Investigations of round vertical turbulent buoyant jets. J Fluid Mech 195:341–391. https://doi.org/10.1017/S0022112088002447
39. Pitts DR, Sissom LE (1998) Schaum's outline of theory and problems of heat transfer. McGraw-Hill, New York. ISBN: 960-8050-39-5
40. Patankar SV (1980) Numerical heat transfer and fluid flow. McGraw-Hill, New York. ISBN 978-0891165224
41. Hunt GR, Linden PF (2001) Steady-state flows in an enclosure ventilated by buoyancy forces assisted by wind. J Fluid Mech 426:355–386. https://doi.org/10.1017/S0022112000002470
42. Stefanidou MK, Bloutsos AA, Yannopoulos PC (2021) Effect of non-axial velocity component on the mean axial velocity measurements in thermal plumes using an air velocity transducer. In: e-Proceedings of the 9th international symposium on environmental hydraulics, 18–22 July 2021, Seoul, Republic of Korea
43. Yannopoulos PC (2006) An improved integral model for plane and round turbulent buoyant jets. J Fluid Mech 547:267–296. https://doi.org/10.1017/S0022112005007263
44. Yannopoulos PC (2010) Advanced integral model for groups of interacting round turbulent buoyant jets. Environ Fluid Mech 10(4):415–450. https://doi.org/10.1007/s10652-010-9173-0
45. Yannopoulos PC, Bloutsos AA (2012) Escaping mass approach for inclined plane and round buoyant jets. J Fluid Mech 695:81–111. https://doi.org/10.1017/jfm.2011.564
46. Yannopoulos PC, Noutsopoulos GC (2006) Interaction of vertical round turbulent buoyant jets—part II: superposition method. J Hydraul Res 44(2):233–248. https://doi.org/10.1080/00221686.2006.9521678
47. Yannopoulos PC (2012) Unique superposition solution of multiple plane or round buoyant jets for tracer and buoyancy fluxes. J Environ Eng 138(9):985–989. https://doi.org/10.1061/(ASCE)EE.1943-7870.0000554
48. Yannopoulos PC (2017) Unique superposition solution of multiple plumes' flow via mean kinetic energy fluxes. J Hydraul Eng. https://doi.org/10.1061/(ASCE)HY.1943-7900.0001361
49. Batchelor GK (2000) An introduction to fluid dynamics. Cambridge University Press, Cambridge. ISBN: 9780511800955

50. Marshall JS (2001) Inviscid incompressible flow. Wiley, New York. ISBN: 0-471-37566-,
51. Yannopoulos PC (2011) Integral model for the reattachment of two interacting turbulent buoyant jets. In: Proceedings of the VII international symposium on stratified flows (ISSF 2011), August 22–26, 2011, Rome, Italy; Editors: A. Cenedese, St. Espa, R. Purini; No. 1239, 8 p
52. Lai ACH, Lee JHW (2012) Dynamic interaction of multiple buoyant jets. J Fluid Mech 708:539–575. https://doi.org/10.1017/jfm.2012.332
53. Chigier NA, Beér JM (1964) The flow region near the nozzle in double concentric jets. Trans ASME J Basic Eng D 86:797–804. https://doi.org/10.1115/1.3655957
54. Miller DR, Comings EW (1960) Force-momentum fields in a dual-jet flow. J Fluid Mech 7:237–256. https://doi.org/10.1017/S0022112060001468
55. Ayukawa K, Shakouchi T (1976) Analysis of a jet attaching to an offset parallel plate. Bull JSME 19(130):395–401. https://doi.org/10.1299/jsme1958.19.395
56. Hunt GR, Kaye NB (2005) Lazy plumes. J Fluid Mech 533:329–338. https://doi.org/10.1017/S0022112005004577X
57. NASA, U. S. Standard Atmosphere. Report NOAA-S/T 76-1562, National Oceanic and Atmospheric Administration, National Aeronautics and Space Administration, United States Air Force, Washington D.C., October 1976, Air density calculator at https://www.digitaldutch.com/atmoscalc/index.htm (1976)
58. BARANI DESIGN Technologies, Air density calculator. http://www.wind101.net/air-density/air-density-calculator.htm/ (2012)
59. Ogino F, Takeuchi H, Kudo I, Mizushina T (1980) Heated jets discharged vertically into ambients of uniform and linear temperatures profiles. Int J Heat Mass Transf 23:1581–1588. https://doi.org/10.1016/0017-9310(80)90162-3
60. Baines WD, Turner JS (1969) Turbulent buoyant convection from a source in a confined region. J Fluid Mech 37(1):51–80. https://doi.org/10.1017/S0022112069000413
61. Caulfield CP, Woods AW (2002) The mixing in a room by a localized finite-mass-flux source of buoyancy. J Fluid Mech 471:33–50. https://doi.org/10.1017/S0022112002002082
62. Hunt GR, Kaye NB (2004) On transient flow in a ventilated filling box. In: 15th Australasian fluid mechanics conference. The University of Sydney, Sydney, Australia, 13–17 December 2004, 4 p
63. Olver PJ (2014) Introduction to partial differential equations. Undergraduate texts in mathematics. Springer, New York
64. Olver PJ (2022) Complex analysis and conformal mapping. University of Minnesota, Minneapolis
65. Wallace RB, Wright SJ (1984) Spreading layer of two-dimensional buoyant jet. J Hydraul Eng 110(6):813–828. https://doi.org/10.1061/(ASCE)0733-9429(1984)110:6(813)